Loss of E3 ligase *HvST1* function substantially increases recombination

Jamie Orr[1*], Sybille Mittmann[1,2*], Luke Ramsay[1], Dominika Lewandowska[1], Abdellah Barakate[1], Malcolm Macaulay[1], Nicola McCallum[1], Robbie Waugh[1,2] and Isabelle Colas[1]. ***Authors contributed equally to this work***

1. Cell and Molecular Sciences, The James Hutton Institute, Invergowrie, Dundee, Scotland DD2 5DA, UK.
2. Division of Plant Sciences, University of Dundee at The James Hutton Institute, Invergowrie, Dundee, Scotland DD2 5DA, UK.

Corresponding author: Isabelle Colas **Email:** Isabelle.Colas@hutton.ac.uk

ORCIDs

Jamie Orr 0000-0003-3125-687X
Sybille Mittmann 0000-0001-6168-2429
Luke Ramsay 0000-0003-2209-2308
Dominika Lewandowska 0000-0002-4734-2791
Abdellah Barakate 0000-0002-7628-6741
Malcolm Macaulay 0000-0002-9008-0053
Nicola McCallum 0000-0002-9438-1697
Robbie Waugh 0000-0003-1045-3065
Isabelle Colas 0000-0001-6980-9906

Keywords: Barley, Crossover, Ubiquitin, Meiosis, Recombination

Word count 7,510

Summary

During meiosis, genetic recombination occurs via repair of DNA double-strand breaks (DSBs) as crossovers (COs) resulting in the exchange of parental genetic material (De Muyt *et al.,* 2009). Crossovers are important for chromosome segregation and shuffling genetic variation, but their number and distribution are tightly regulated (Zickler and Kleckner, 2015). In barley and other large genome cereals, recombination events are limited in number and mainly restricted to the ends of chromosomes (Mascher *et al.,* 2017), constraining progress in plant breeding. Recent studies have highlighted subtle differences in meiotic progression (Higgins *et al.,* 2012; Phillips *et al.,* 2013) and the distribution of recombination events in barley compared to other plants (Colas *et al.,* 2016; Colas *et al.,* 2017; Colas et al 2019), indicating possible evolutionary divergence of the meiotic program in large genome crops. Here we identify a spontaneous loss of function mutation in the grass specific E3 ubiquitin ligase *HvST1* (*Sticky Telomeres 1*) which results in semi-sterility in barley. We show that abnormal synapsis in the absence of HvST1 function increases overall recombination by up to 2.5-fold and that HvST1 is capable of ubiquitinating ASY1, a key component of the lateral elements of the synaptonemal complex. Our findings shed light on an evolutionarily divergent pathway regulating synapsis and recombination in cereals. This natural loss of function variant presents new opportunities for the modulation of recombination in large genome cereals.

Introduction

Homologous recombination (HR) through resolution of double strand breaks (DSBs) as crossovers (COs) is an important trait for breeders, who rely on this mechanism of genetic exchange during meiosis to create novel crop varieties. In barley, HR occurs mainly in distal chromosome regions leaving large sections of the genome almost devoid of recombination (Kunzel *et al.,* 2002; Lambing *et al.,* 2018). In plants, pairing of replicated homologous chromosomes in meiosis I is guided by the formation of DSBs catalyzed by SPO11-1 and SPO11-2 (Grelon *et al.,* 2001; Hartung *et al.,* 2007). One strand of DNA at each side of the DSB is partially degraded (resected) by the MRE11-Rad50-NSB1 complex leaving 3' single stranded DNA (Daoudal-Cotterell *et al.,* 2002; Wang *et al.,* 2014). The RECA protein family, which includes RAD51 and DMC1 proteins, mediate strand invasion to create a "D-loop" (Pradillo *et al.,* 2012; Da Ines *et al.,* 2013). It is postulated that D-Loops in plants are resolved through double-Holliday junction (dHj) recombination intermediates to make COs (Neale *et al.,* 2006) via one of two pathways, resulting in either class I or class II COs. Class I CO resolution depends on the ZMM proteins (Zip1-4, Msh4/Msh5, and Mer3) (Higgins *et al.,* 2005; Higgins *et al.,* 2008b) and is subject to CO interference, a phenomenon that restricts the proximity of DSBs repaired as COs via this pathway (Capilla-Perez *et al.,* 2021). Class II CO resolution is thought to depend on the MUS81 pathway (Higgins *et al.,* 2008a) and is not subject to CO interference (Falque *et al.,* 2009). In Arabidopsis and barley, it is estimated that only 5% of DSBs are resolved as COs (Serra *et al.,* 2018, Higgins *et al.,* 2012) and that 85% of these are resolved through the interference sensitive class I pathway. This introduces significant linkage drag which limits the ability of barley breeders to separate desirable and undesirable traits. The barley

secondary gene pool—land races and wild relatives—are a valuable resource to breeders for novel traits such as disease or drought resistance. However, linkage drag can impose a severe yield or quality penalty when attempting to transfer these traits to elite varieties. Therefore, the ability to increase recombination and break interference is appealing to plant breeders.

At the onset of meiosis in barley the telomeres cluster to one side of the nucleus and the formation of the synaptonemal complex (SC, synapsis) is initiated (Higgins *et al.,* 2012, Colas *et al.,* 2017). The SC is a tri-partite structure consisting of two lateral elements which form along replicated sister chromatids, helping to constrain them, and a central element which, beginning from the clustered telomeric region, forms between the lateral elements helping to physically link the paired homologous chromosomes during prophase I (Orr *et al.,* 2021a). The SC is later dissolved prior to the first meiotic division, leaving the chromosomes held together by chiasma—the cytogenetic manifestation of COs—which help to ensure correct chromosome segregation during the second round of meiotic division (Orr *et al.,* 2021a). Synapsis can be visualized using antibodies against key SC proteins such as ASY1, a component of the lateral elements, and ZYP1, a component of the central element (Colas *et al.,* 2017). Impairing the recombination pathway not only affects crossover outcomes but can also affect synapsis, demonstrating the tight interplay of the two parallel mechanisms (Grey *et al.,* 2022). However, similar disruptions to these pathways can result in substantial differences in meiotic phenotype in different plant species. For example, barley desynaptic *des10*, which carries a mutation in MLH3 (Colas *et al.,* 2016) displays abnormal synapsis contrary to the equivalent mutation in Arabidopsis (Jackson *et al.,* 2006; Colas *et al.,* 2016).

Recent studies have reported that mutations affecting the function or expression of *FANCM*, *RECQ4* and *HEI10* genes have the potential to increase recombination (Serra *et al.,* 2018; Mieulet *et al.,* 2018; Arrieta *et al.,* 2021) which is of great interest in large genome crops such as barley where the distal bias for recombination events is particularly pronounced (Kunzel *et al.,* 2002; Lambing *et al.,* 2018). To this end, we have exploited a collection of 15 *desynaptic* mutants that have been initially cytologically classified by their chromosome behaviour at metaphase I in the early 1970s (Hernandes-Soriano, 1973). Here we show that one of these lines—BW233—is mutated in the RING domain of a grass specific E3 ubiquitin ligase, that we call *HvST1* (*Sticky Telomeres 1*). We have shown that HvST1 is a functional E3 ubiquitin ligase and is capable of ubiquitinating ASY1 in vitro. Despite an abnormal synapsis progression, we found that loss of E3 ubiquitin ligase activity in *Hvst1* leads to an overall increase recombination which could be exploited during breeding programs.

Materials and Methods

Plant material

H. vulgare BW233 is one of a collection near isogenic lines (NILs) derived from a collection of 15 *desynaptic* mutants that have been initially cytologically classified by their chromosome behaviour at

104 metaphase I in the early 1970s (Hernandes-Soriano, 1973). These mutants have been backcrossed to
105 a common barley cultivar Bowman to create NILs and initially genotyped to find the causal mutation for
106 their meiotic phenotype (Lundqvist *et al.,* 1997; Druka *et al.,* 2010). Barley cv. Bowman and NIL BW233
107 plants were grown under the following conditions: 18-20°C for 16 hours of light and 14-16°C for 8 hours
108 of dark. For cytology, spikes of 1.4 to 2.5 cm were collected, and anthers were prepared as previously
109 described (Colas *et al.,* 2016) For fine mapping, 12 seeds from each of the 16 families of the F_2
110 population of BW233 x Barke were grown in 24-pot trays. For the F_3 recombination assay, 48 families
111 of the harvested F_2 BW233 x Barke population plants were chosen according to their genotypes across
112 the *des12* interval. For the cultivar Barke and BW233 genotypes, 8 seeds per family were sown and
113 grown as described for the F_2 population (24 families per genotype). DNA was extracted from young
114 leaf tissue (two-leaf stage) using the Qiagen DNeasy 96 well plate Kit with the automated station
115 QIAxtractor® or QIAcube®. RNA was extracted from 50 anthers in prophase I, using the Qiagen
116 RNeasy Mini Kit. RNA quantity and quality were assessed with the NanoDrop 2000.

117 ***Cytology***

118 Metaphase spreads were performed as described by Higgins *et al.* (2012) with minor changes. Briefly,
119 fixed anthers were incubated in 1% cellulase and 2% Pectolyase solution at 37°C for 30 minutes. The
120 reaction was stopped by replacing the enzyme mix with cold (4°C) sterile distilled water. Nuclei
121 preparation for immuno-cytology and Immuno-FISH was performed as previously described (Colas *et*
122 *al.,* 2016)

123 *Fluorescence in situ hybridization (FISH):* Probes for Centromeres (Bac7) and Telomeres (HvT01) were
124 amplified by PCR and labelled by nick translation with Alexa-Fluor as previously described (Colas *et al.,*
125 2016). Hybridization mix and denaturation was performed as previously described (Arrieta *et al.,* 2021).
126 Slides were washed in 2xSSC at room temperature (RT) for 10 minutes before digestion with 0.01%
127 (w/v) pepsin in mildly acidified SDW for 45 to 90 seconds at 37°C. Slides were dehydrated using a
128 series of ethanol concentrations (50%, 70%, 90% to 100%) for 2 minutes each and left to air-dry at RT.
129 Hybridization mix (40 µl) was applied to the slides, and slides were incubated at 75°C for 4 minutes,
130 then over night at 37°C in a dark humid chamber. Slides were washed and prepared as previously
131 described (Colas *et al.,* 2016)

132 *Immunocytology:* Slides were prepared as previously described (Colas *et al.,* 2016). The primary
133 antibody solution consisted of one or multiple antibodies; anti-AtASY1 (rabbit, 1:1000), anti-AtZYP1
134 (rat, 1:500), anti-AtDMC1 (rabbit, 1:500), anti-HvMLH3 (rabbit, 1:500), anti-HvHei10 (rabbit, 1:500),
135 diluted in blocking solution (1X PBS with 5% Donkey/Goat serum). For Immuno-FISH, slides were
136 washed in 2x SSC for 5 minutes after the secondary antibody incubation, followed by 10 minutes in 1x
137 PBS. Slides were then fixed with 1% PFA for 10 minutes, rinsed briefly in 1xPBS before following the
138 FISH protocol described earlier from the dehydration step.

139 *Microscopy and Imaging:* 3-dimensional Structured Illumination Microscopy (3D-SIM) and confocal
140 images were acquired on a DeltaVision OMX Blaze (GE Healthcare) and LSM-Zeiss 710 respectively,
141 as previously described (Colas *et al.,* 2016). Images were de-convolved with Imaris deconvolution
142 module Clearview 9.5 and processed for light brightness/contrast adjustment with Imaris 9.5 (Randall
143 *et al.,* 2022*).*

144 ***Positional gene identification***

145 Initial genetic mapping used a custom 384 SNP genotyping array using the Illumina beadXpress
146 platform on an F_2 segregating population derived from a cross between BW233 (*des12.w*) and *cv*.
147 Morex, using the segregation of the semi-sterile phenotype of *des12.w* as a Mendelian trait (Druka *et*
148 *al.,* 2010). The *des12.w* interval was delineated a 1.0 cM interval on chromosome 7HL, by SNP
149 markers found in MLOC_38602 and MLOC_67621. The region was further delineated using custom
150 designed KASPar SNP assays on 960 plants of the segregating F_2 population. KASPar assays were
151 designed based on SNPs extracted from the manifest files of a 9k iSelect Genotyping platform
152 developed at the James Hutton Institute (Bayer *et al.,* 2017). Synteny with rice and *Brachypodium* was
153 used to identify genes that would be useful for delineation of the interval and contigs from cvs. Morex,
154 Bowman and Barke. Assemblies were pulled out using the cDNA of the gene sequence, gathered
155 from Ensembl Plants (Bolser *et al.,* 2017) and BARLEX (Colmsee *et al.,* 2015). BACs that contained
156 the 9 significant genes in the *des12.w* interval were obtained from the HarvEST web server (Close *et*
157 *al.,* 2009) to find sequences of interest to BLAST, sequence, and identify any polymorphisms between
158 BW233 and WT alleles (from cultivars Bowman, Barke, Morex, Freya, and Glages). Linkage maps were
159 constructed using the combined genotypic and phenotypic data described above using JoinMap 4.1
160 (Stam, 1993).

161 ***F_3 recombination assay***

162 The F_3 recombination assay was based on KASP™ genotyping chemistry using 48 markers spanning
163 3 chromosomes (1H, 5H, and 6H; Table S1). The selected markers and frozen leaf punches were
164 sent to LGC for KASP assay development. Data was visualised with Flapjack (Milne *et al.,* 2010) and
165 further analysed in Microsoft Windows Excel 2013. Recombination frequencies were calculated to
166 generate linkage maps with MapChart (Voorrips *et al.,* 2002). A subset of the F_3 families was
167 subsequently analysed with the barley Illumina iSelect 50k SNP array (Bayer *et al.,* 2017).
168 Monomorphic markers were removed, and a sliding window was used to correct for poorly mapped
169 markers. F_2 recombination events, visible as large monomorphic blocks, generated unusually high
170 crossover counts for individual markers, markers with crossover counts above 5 across all 95 plants
171 were removed to account for this. All code used in 50K analysis and plotting is available online (see
172 code availability statement).

173 **Gene model and expression**

174 The *HvST1* gene model was constructed using the Barley Reference Transcriptome (BaRT) v2.18
175 (Coulter *et al.,* 2022). HvST1 meiotic expression was plotted using data from the Barley Anther and
176 Meiocyte Transcriptome (BAnTr) (Barakate *et al.,* 2021).

177 **Gene Cloning**

178 *HvST1,* truncated *Hvst1*, and *HvASY1* cDNA was synthesised with the SuperScript® III First- Strand
179 Synthesis System (Invitrogen) using the included oligo(dT) primer. cDNA was then amplified using
180 nested PCR (Primers in Table S2) with High-Fidelity Phusion or Q5 DNA polymerase (New England
181 Biolabs), and the PCR products ligated into pGEM®-T Easy vector (Promega). Competent cells of *E.*
182 *coli* JM109 were transformed with the ligations and plated on solid LB medium containing Ampicillin,
183 X-gal, and IPTG for selection and blue-white screening. Plasmid DNA was purified from positive clones
184 using the QIAprep Spin Miniprep Kit (Qiagen). The cDNA sequence was verified by Sanger sequencing
185 using T7 and SP6 primers.

186 **Protein Expression Constructs**

187 *HvST1,* truncated *Hvst1*, and *HvASY1* coding regions were amplified from respective pGEM-T plasmids
188 by PCR using primers with attB1 and attB2 Gateway sites (Table S3). The TEV protease cleavage site
189 was introduced by overlapping TEV-oligonucleotide and the PCR product cloned into pDONR207 using
190 BP clonase (Invitrogen). The resulting BP clonase reaction was transformed into *E. coli* DH5α chemical
191 competent cells (ThermoFisher Scientific). The transformation was plated on LB agar plates containing
192 25 µg/ml gentamycin. After colony PCR screening with attB1 and attB2 primers, overnight cultures of
193 the positive clones were prepared in LB medium with 25 µg/ml gentamycin and their plasmid DNA
194 prepared and verified by Sanger Sequencing using PDONR207 forward and reverse primers. The
195 *HvST1* insert was then transferred into pDEST-HisMBP (Nallamsetty *et al.,* 2009) using LR clonase
196 (Invitrogen)[21]. The LR clonase reaction was used to transform *E. coli* DH5α competent cells before
197 plating on LB agar plates supplemented with 100 µg/ml ampicillin. Plasmid DNA of positive clones was
198 prepared and checked by restriction digest using HincII for *HvST1/Hvst1* and BamHI and BglII (New
199 England Biolabs) for *HvASY1*. The selected clones were then transferred into *E. coli* Rosetta™ 2(DE3)
200 pLysS (Novagen). The transformations were plated on LB agar plates supplemented with 100 µg/ml
201 ampicillin and 34 µg/ml chloramphenicol. A single colony was grown overnight in LB medium with both
202 antibiotics.

203 **Protein Expression and Purification**

204 Single colonies from successful transformants were grown to OD600 nm of approximately 0.6 in LB
205 with of 100 µg/ml Ampicillin and 34 µg/ml Chloramphenicol at 37°C and 220 rpm. Cultures were cooled
206 on ice before induction with 0.1 mM IPTG and grown overnight at 18°C and 220 rpm. Induced cells
207 were then pelleted by centrifugation, flash frozen in liquid nitrogen, and stored at -80°C until use.
208 Induced cell pellets were lysed in BugBuster® Master Mix (Novagen) with cOmplete™ the EDTA-free
209 Protease Inhibitor Cocktail (Roche). The overexpressed protein was purified using HisPur NiNTA resin

210 (ThermoFisher). For removal of the HisMBP tag, NiNTA elution buffer was exchanged with 50 mM
211 TrisHCl, pH 8.0 using Pierce 10K MWCO spin columns (ThermoFisher) before digestion with ProTEV
212 Plus (Promega) overnight at 4°C with the addition of 1% Triton X-100. Detergent was removed using a
213 Pierce detergent removal spin column (ThermoFisher), then a second round of NiNTA capture removed
214 the cleaved tag, leaving the purified protein in the spin column flow through. Purified protein was
215 exchanged into PBS (pH 7.4) using Slide-A-Lyzer G2 dialysis cassettes (ThermoFisher) and stored at
216 4°C until use. The concentration of the purified protein was measured using the Pierce 660 nm
217 microplate assay (ThermoFisher) and absorbance read on the Varioskan Lux (ThermoFisher).

218 ***In vitro* ubiquitination assays**

219 Purified HvST1 interactions with E2 conjugating enzymes were determined by screening against a
220 panel of human E2 conjugating enzymes using the E2-scan plate (Ubiquigent). Reactions were
221 evaluated for accumulation of polyubiquitinated products via SDS-PAGE followed by staining with
222 SimplyBlue Safe Stain (ThermoFisher) and western blotting with mouse anti-ubiquitin conjugate
223 antibody at a dilution of 1:10000 (Ubiquigent). Subsequent ubiquitination time course assays were
224 conducted using histidine tagged UBE1, UBE2D4, bovine ubiquitin, and 8 mM ATP (Ubiquigent). HvST1
225 autoubiquitination time course assays and substrate (HvASY1) ubiquitination assays were incubated at
226 37°C for between 0 and 60 minutes. All control reactions were incubated at 37°C for 60 minutes.

227 These reactions were analysed via SDS-PAGE followed by SimplyBlue Safe Stain (ThermoFisher) and
228 western blotting using mouse anti-ubiquitin conjugate antibody as above, rat anti-HvST1 antibody
229 (1:200), mouse anti-^{6}His antibody (1:10000; ThermoFisher), and rabbit anti-HvASY1 antibody (1:5000;
230 Agrisera; this study; AS21 4690). Excised gel fragments from autoubiquitination experiments were
231 prepared as previously described (Lewandowska *et al.,* 2019). Mass spectrometry was carried out by
232 Dundee University FingerPrints Proteomics Facility. The resulting raw files were processed and
233 searched using MaxQuant (v1.6.10.43) (Tyanova *et al.,* 2016) and the Andromeda peptide search
234 engine (Cox *et al.,* 2008, Cox *et al.,* 2011) against the E. coli BL21 RefSeq proteome
235 (GCF_014263375.1) combined with a custom set of sequences for the purified proteins added to the
236 assay.

237 **TUBE capture**

238 GST-tagged tandem ubiquitin binding entities (GST-TUBEs) were expressed and purified as described
239 by Skelly *et al.* (2019) The HvASY1 ubiquitination assay was prepared as above and incubated for two
240 hours at 37°C. The reaction was passed through a 50 KDa size exclusion column (ThermoFisher) to
241 eliminate remaining free ubiquitin. GST-TUBE was added to the column retentate to a final
242 concentration of 200 µg/ml before overnight glutathione agarose (ThermoFisher) capture at 4°C with
243 gentle agitation. Each fraction of the glutathione agarose capture was retained and of equal volume.
244 The captured protein was divided in two and half was incubated for two hours at 37°C with broad

245 spectrum deubiquitinating enzyme (DUB; LifeSensors). The results of the assay were determined via
246 SDS-PAGE and western blotting as described above.

247 **CRISPR/Cas9 construct**

248 To find suitable CRISPR/Cas9 knockout targets in the *HvST1* gene, the coding sequence was
249 searched using the online algorithm at http://www.broadinstitute.org/rnai/public/analysis-tools/sgrna-
250 design. Two spacer sequences of 20 nucleotide with the highest score and a guanine at their 5' end
251 as transcription start and preferably an A or G at the 3' end for increased CRISPR/Cas9 efficiency were
252 selected. A search for potential off-targets was performed using the barley genes database developed
253 at the James Hutton Institute (https://ics.hutton.ac.uk/barleyGenes/index.html). Two complementary
254 oligonucleotides of 20 nucleotides were designed for each target with an additional 4 nucleotides at
255 their 5'-end for cloning into AarI restriction sites in the destination vector pBract214m-HvCas9-HSPT.
256 This vector contains a barley codon optimised Cas9 (HvCas9) under the control of maize ubiquitin
257 promoter and *Arabidopsis* heat shock protein 18.2 terminator and sgRNA scaffold under the control of
258 rice small nuclear RNA (snRNA) U6 promoter (OsU6p). The complementary oligonucleotides (Table
259 S 4) were annealed using equal amounts of each oligo. Oligonucleotide mixtures were heated in
260 boiling water then left to cool to room temperature. 1 µl of duplex DNA was ligated into 25 ng of
261 pBract214m-HvCas9-HSPT vector linearized with AarI using the ligation reagents and protocol
262 described in pGEM®-T Easy Vector System kit (Promega). The ligation reaction was incubated
263 overnight at 4°C then transformed into competent *E. coli* DH5α strain (New England Biolabs) and
264 plated on LB medium containing 25 µg/ml Kanamycin. Inserts were verified by colony PCR and Sanger
265 sequencing as described above. Additionally, the integrity of the plasmids was checked by digestion
266 with restriction enzyme BglI (Thermo Fisher Scientific). The plasmid DNA was then transformed into
267 *Agrobacterium tumefasciens* AGL1 strain containing replication helper pSoup
268 (http://www.bract.org/constructs.htm#barley) by electroporation. Briefly, 50 µl electro-competent
269 Agrobacterium AGL1/pSoup was thawed on ice, 1 µl plasmid DNA was added, and the mixture was
270 transferred to an electroporation cuvette and pulsed at 2.5 Kv. 1 ml YEB medium was added and the
271 mixture was transferred into 15 ml falcon tube (Sigma Aldrich) and incubated at 28°C shaking at 200
272 rpm for 2–3 h before plating on LB agar supplemented with 50 µg/ml Kanamycin (Merck Millipore). The
273 plates were incubated for 2– 3 days at 28°C. Transformed *Agrobacterium* clones from each CRISPR
274 construct were grown in YEB medium and used to transform barley Golden Promise immature embryos
275 (Bartlett *et al.,* 2008) in the plant transformation facility at The James Hutton Institute. Transgenic plants
276 containing CRISPR constructs were regenerated under hygromycin selection.

277 **CRISPR/Cas9 screening and genotyping**

278 For screening the T0 CRISPR plants, 2mm leaf discs were collected in 20 µl Phire Plant PCR Buffer
279 (Thermo Fisher Scientific) and crushed with a 100 µl pipette tip. For construct CRISPR01 genotyping,
280 the KAPA3G Plant PCR Kit (Sigma-Aldrich) was used to amplify an 824 bp fragment spanning the gene
281 target site using an initial touchdown for 6 cycles with annealing at 70°C decreasing by 1.6°C per cycle
282 followed by 34 cycles annealing at 62.1°C. An amplicon for construct CRISPR02 was amplified with the

283 Phire Plant Direct PCR kit using an initial touchdown annealing for 8 cycles starting at 72°C and
284 decreasing by 0.9°C per cycle followed by 31 cycles annealing at 65.4°C. Products were sequenced
285 by Sanger Sequencing as described above to verify potential mutations. Based on sequencing data, 8
286 individuals were identified that had mutations at the expected gene location for the CRISPR01
287 construct. 20 seeds of each were sown in 24-pot trays soil in the glasshouse. At the two-leaf stage, 2
288 mm leaf discs were collected, and plants were genotyped to identify plants that were homozygous for
289 the identified mutations as described above. Additionally, plants were screened by PCR and gel
290 electrophoresis for the presence or absence of the Cas9 transgene with Cas9-F2 and Cas9-R2 primers
291 (Table S5). Five plants originating from three different T0 plants were identified to be homozygous and
292 contain no Cas9 transgene. These lines were re-potted in 9-inch pots of soil to generate more seeds
293 and tillers for cytology analysis. As control two plants that were found to contain no mutations were
294 also included. Plants were grown for 6 weeks until they reached meiosis and inflorescences were
295 collected for chromosome spreads and immunolocalization as described above.

296 **Phylogenetic analysis**

297 Proteomes from barley (*H. vulgare*), rice (*O. sativa*), wheat (*T. aestivum*), maize (*Z. mays*), tomato (*S.*
298 *lycopersicum*), cassava (*M. escualenta*), pineapple (*A. comosus*), soybean (*G. max*), clementine (*C.*
299 *clementina*), *Brassica oleracea*, Tabaco (*N. tabacum*), *Arabidopsis thaliana*, *Amborella trichopoda*,
300 *Physcomitrella patens*, yeast (*S. cerevisiae*), *C. elegans*, *D. melanogaster*, zebrafish (*D. rerio*), human
301 (*H. sapiens*), mouse (*M. musculus*), and clawed frog (*X. laevis*) were clustered into ortholog groups
302 using Orthofinder (Emms and Kelly, 2019; v2.3.3). HvST1 clustered only with proteins from included
303 Poaceae proteomes. Further potential orthologs within Poaceae and the best possible alignments within
304 *Arabidopsis* and monocot spp. were determined by BLAST alignment to the non-redundant archive
305 (Altschul *et al.,* 1990) and larger EggNOG (Huerta-Cepas *et al.,* 2019; v5.0) pre-computed orthologous
306 groups. The longest isoforms of these proteins were aligned using MAFFT (Katoh *et al.,* 2002; v7.266),
307 and maximum likelihood phylogeny constructed using IQ-TREE (Minh *et al.,* 2020; v2.0.3) using model
308 JTT+G4 with ultrafast bootstrapping (n=1000). The resultant phylogeny was visualised using ggtree
309 (Yu, 2020) (v.2.5.1).

310 ## Results

311 **The *des12.w* phenotype is due to a frame shift mutation in a novel E3 ubiquitin ligase**

312 BW233 *(des12.w)* is semi-sterile isogenic line of the barley cv. Bowman (Fig. 1a) that carries a
313 spontaneous mutation which originated in *cv*. Freja. In contrast to Bowman (wild type; WT) metaphase
314 I (Fig. 1b), BW233 metaphase I (Fig. 1c) chromosomes are sticky and often interlocked in telomeric
315 regions (arrows) and a statistically significant increase in mean rod-bivalent and decrease in mean ring
316 bivalent chromosomes (T-test, Benjamini and Hochberg corrected p = 0.024 for both) are observed
317 (Fig. 1d and Fig. S1). Chiasma counts from Bowman (n=19) and BW233 (n=44) meiocytes at
318 metaphase I showed a significant decrease in BW233 chiasma (Wilcoxon rank sum test, p=0.0055) and
319 altered distribution compared to Bowman (Fig. S2). Chromosomes interlocks often persist at anaphase

320 I (Fig. 1e) and anaphase II in BW233 meiocytes (Fig. 1f), potentially causing lagging chromosomes and
321 mis-segregation.

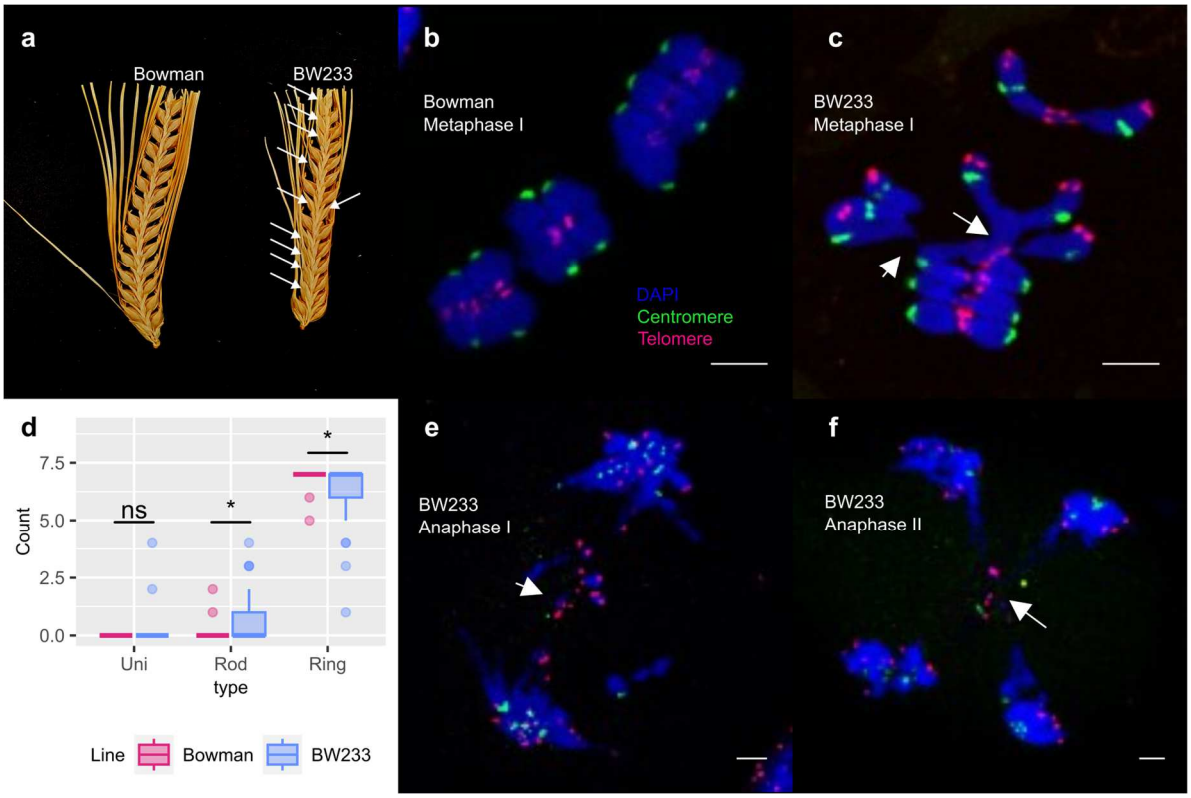

322

Figure 1: BW233 phenotype

a) Spike fertility comparison between Bowman and BW233, with missing seed indicated by white arrows. b) Bowman metaphase I with 7 ring bivalents. c) BW233 metaphase I, with 7 bivalents often interlocked at the telomere region (white arrows). d) Box plot of univalent, rod bivalent, and ring bivalent counts in *HvST1* and *Hvst1* plants with significance (T-test) indicated above. e) BW233 anaphase I, showing lagging chromosomes and chromosomes bridges (white arrow). f) BW233 anaphase II with interlocked chromosomes at the telomere region (white arrow). DAPI (blue), telomeres (red), centromeres (green). Scale bar 5 µm

323

324 To find the causal mutation of the *des12.w* phenotype, we used F_2 populations of two crosses — BW233
325 x *cv*. Barke and BW233 x *cv*. Morex — scoring semi fertility as the segregating phenotype (Fig. 1a). We
326 initially mapped the *des12.w* mutation to the long arm of chromosome 7H (Druka *et al.,* 2011) and by
327 positional cloning (Fig. S3) identified a short exonic mononucleotide microsatellite in
328 HORVU7Hr1g092570 (Morex v3: HORVU.MOREX.r3.7HG0722700) (Mascher *et al.,* 2021) that
329 contains an extra guanine in BW233 compared to WT cultivars Bowman, Barke, Freja, Morex, and
330 Betzes, which induces a frameshift (Fig. 2a and Fig. S4). HORVU.MOREX.r3.7HG0722700 is a 990 bp
331 single exon gene encoding a 330 amino acid RING finger domain containing putative E3 ubiquitin ligase
332 (34) that we have named *STICKY TELOMERES 1* (*HvST1*) (Fig. S4). The frame shift in *des12.w* (*Hvst1*)
333 introduces a premature termination codon in *HvST1* that eliminates the RING domain and compromises
334 gene function (Fig. 2a and Fig. S4). In our 'barley anther and meiocyte transcriptome' (Barakate *et al.,*

335 2021) dataset, we found that *HvST1* expression was significantly enriched in staged meiocytes when
336 compared to anthers, rising to peak expression in pachytene–diplotene (Fig. 2b). Sequencing RT-PCR
337 products from WT and BW233 (*Hvst1*) anthers revealed that *HvST1* and *Hvst1* produced mRNA
338 encoding 330 and 298 amino acid proteins respectively, confirming the introduction of a premature
339 termination codon in the latter (Fig. 2c and Fig. S4). Screening a further four independent semi-sterile
340 desynaptic mutants (Fig. S5) originating from different cultivars (Betzes, Klages) revealed that they also
341 carried spontaneous mutations in the same microsatellite; BW240 (*des4.af;* from cv Klages), BW241
342 (*des4.a,* from cv Betzes) and BW229 (*des1.v,* from cv Freja) contain the same 1bp insertion, while
343 BW242 (*des4.h,* from cv Betzes) has a 1bp deletion (Fig. S6). We generated CRISPR/Cas9 knockouts
344 of this gene in *cv* Golden Promise which also caused semi-sterility (Fig. S7).

345 **HvST1 is a grass-specific functional ubiquitin Ligase**

346 Clustering and phylogenetic analysis of HvST1 places it within a group of grass-specific proteins (Fig.
347 S8), that includes the rice orthologue CYTOSOL LOCALISED RING FINGER PROTEIN 1 (Park *et al.,*
348 2019) (OsCLR1; Os06g0633500). More recently, Ren *et al*. (2021) reported a study of DESYNAPSIS1
349 (DSNP1), an induced mutation by irradiation that introduced a 2bp deletion in the exonic region of
350 LOC_Os06 g4270, causing a large reduction of crossovers which was already visible at metaphase and
351 sterility (Ren *et al.,* 2021). Alignment of OsCLR1 and DSNP1 revealed that they are identical. Within
352 grasses HvST1/OsCLR1-like proteins shows strong C-terminal conservation—including the RING
353 domain—with a more variable N-terminal region (Fig. S9). Outside of the Poaceae alignment is limited
354 almost entirely to the E2 interacting RING domain. *OsCLR1* is highly expressed under salt and drought
355 stress (Park *et al.,* 2019). However, this is not a trait shared by orthologues in sorghum, maize, and
356 wheat (Park *et al.,* 2019), nor is *HvST1* differentially expressed under these conditions (Fig. S10),
357 suggesting a unique gain of function in rice OsCLR1/DSNP1.

358 RING domain containing proteins comprise the largest group of E3 ubiquitin ligases, which confer
359 substrate specificity to the ubiquitination cascade (Dove *et al.,* 2016). The RING domain allows the E3
360 ligase to recruit E2 conjugating enzymes allowing the transfer of ubiquitin from the E2 to E3-bound
361 protein substrates (Dove *et al.,* 2016; Iconomou and Saunders*.,* 2016). Loss of this domain in *Hvst1*
362 should therefore prevent interaction with E2 conjugating enzymes. In autoubiquitination time course
363 assays, purified HvST1 interacted with the human E1 activating (UBE1) and E2 conjugating enzyme
364 (UBE2D4), producing high molecular weight polyubiquitinated substrates visible via both Coomassie
365 gel staining (Fig. 2d) and western blot with anti-ubiquitin conjugate antibodies (Fig. 2e). Purified *Hvst1*
366 mutant protein did not interact with any E2 (Fig. 2d). Western blotting with anti-HvST1 antibodies
367 confirmed that HvST1 gained mass over the autoubiquitination time course (Fig. 2f). The identity of all
368 protein bands in this assay was further confirmed by mass spectrometry (Fig. S11), confirming the
369 specificity of the HvST1 antibody. Purified HvST1 protein interacted strongly with all human E2
370 conjugating enzymes in the UBE2D and UBE2E families (Fig. S12), and to a lesser extent with UBE2A,
371 UBE2B, and UBE2N/V1. We conclude that HvST1 is a functional E3 ubiquitin ligase and that loss of
372 the RING domain in *Hvst1* leads to loss of E3 ligase activity.

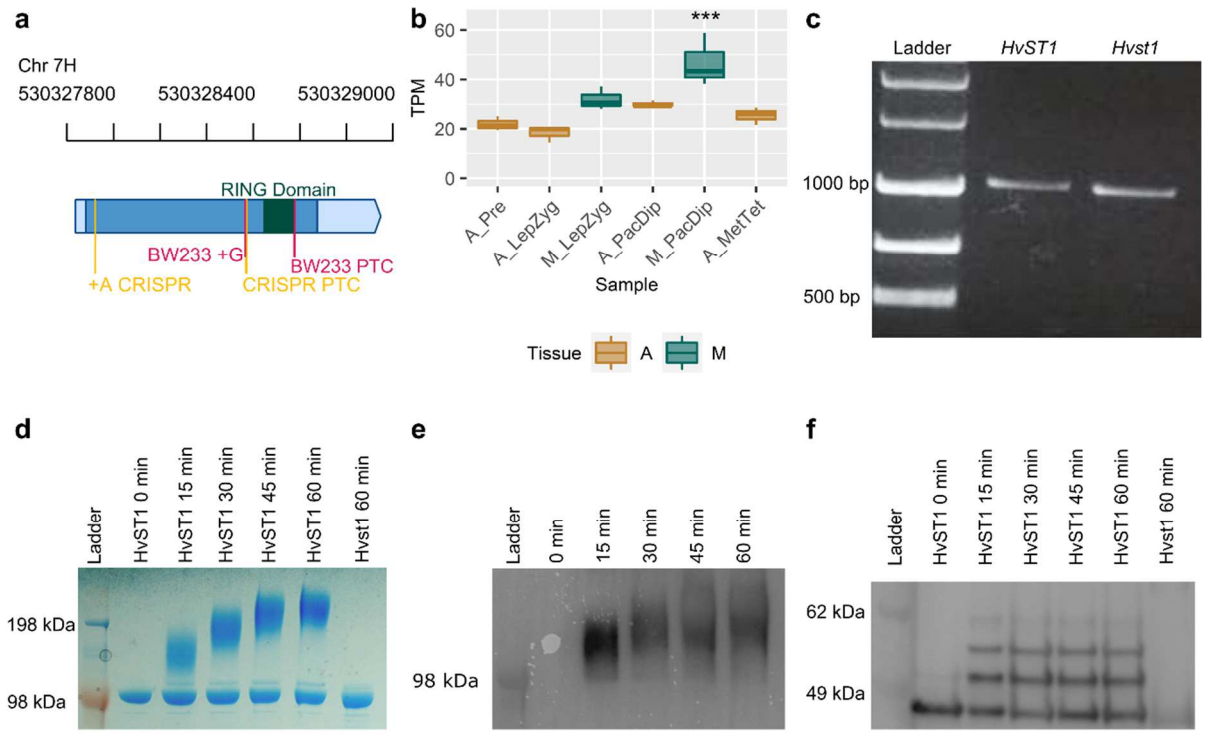

Figure 2: HvST1 characterisation

a) *HvST1* gene model derived from Barley Reference Transcriptome 2 (BaRT2v18; Coulter *et al.,* 2022) RNA sequences mapped to the barley cv Barke genome with the BW233 (*Hvst1)* insertion (+G) and premature termination codon (PTC) indicated in dark pink and the CRISPR/Cas9 insertion and PTC indicated in yellow. The region encoding the RING domain is indicated in dark green. WT 3' and 5' untranslated regions (UTRs) are indicated in light blue while WT coding sequences are indicated in dark blue. The physical genomic coordinates are indicated above. b) Expression profile of *HvST1* in time resolved anther and meiocyte expression data (Barakate *et al.,* 2021) where A=Anther, M=Meiocyte, Pre=pre-meiosis, LepZyg=Leptotene–Zygotene, PacDip=Pachytene–Diplotene, and MetTet=Metaphase–Tetrad. The statistical significance ($p<0.001$) of *HvST1* expression in meiocytes at Pachytene-Diplotene as determined by ANOVA and Tukey's honest significant difference is indicated above the box. c) agarose gel of FL cDNA from RT-PCR of *HvST1* from Bowman and *Hvst1* from BW233 anthers. d) Coomassie stained SDS-PAGE of autoubiquitination time-course assay. e) anti-ubiquitin conjugate probed western blot of HvST1 autoubiquitination time course assay. f) anti-HvST1 probed western blot of autoubiquitination time course assay.

HvST1 mutants exhibit abnormal synapsis

As *Hvst1* mutants are semi-fertile, and display abnormal chromosome segregation (Fig.1), we used Structured Illumination Microscopy (SIM) to compare synapsis progression between the wild type (WT) and *Hvst1* mutants, using antibodies raised against axial (ASY1) and central element (ZYP1) proteins of the synaptonemal complex (SC) (Colas *et al.,* 2017). Axis formation and the initiation of synapsis during early-zygotene were comparable in WT (Fig. 3a) and *Hvst1* (Fig. 3e). By mid-zygotene in the WT most of the chromosomes are paired (Fig. 3b) and the typical tri-partite structure of the SC is visible

382 in the paired region (Philips *et al.,* 2012). In contrast, *Hvst1* meiocytes at the same stage exhibit faltering
383 development with ZYP1 forming abnormal telomeric polycomplex-like clusters (Fig. 3f). At pachytene
384 stage, WT chromosomes are fully synapsed (Fig. 3c) but in *Hvst1* complete synapsis is compromised
385 (Fig. 3g). During diplotene WT chromosomes display a normal tinsel configuration (Colas *et al.,* 2017)
386 as the SC is dissolved (Fig. 3d). However, in *Hvst1*, ASY1 unloading from the SC is perturbed and less
387 organized with apparent misalignment and unpaired regions (Fig. 3h and Fig. S13). The same synapsis
388 defect was observed in insertion mutants BW229, BW240, and knockout Hv*st1*$^{CRISPR/Cas9}$, confirming
389 cytologically that loss of E3 ligase activity in *Hvst1* causes the ZYP1 polycomplex-like phenotype,
390 independently from the original background (Fig. S13 and S14).

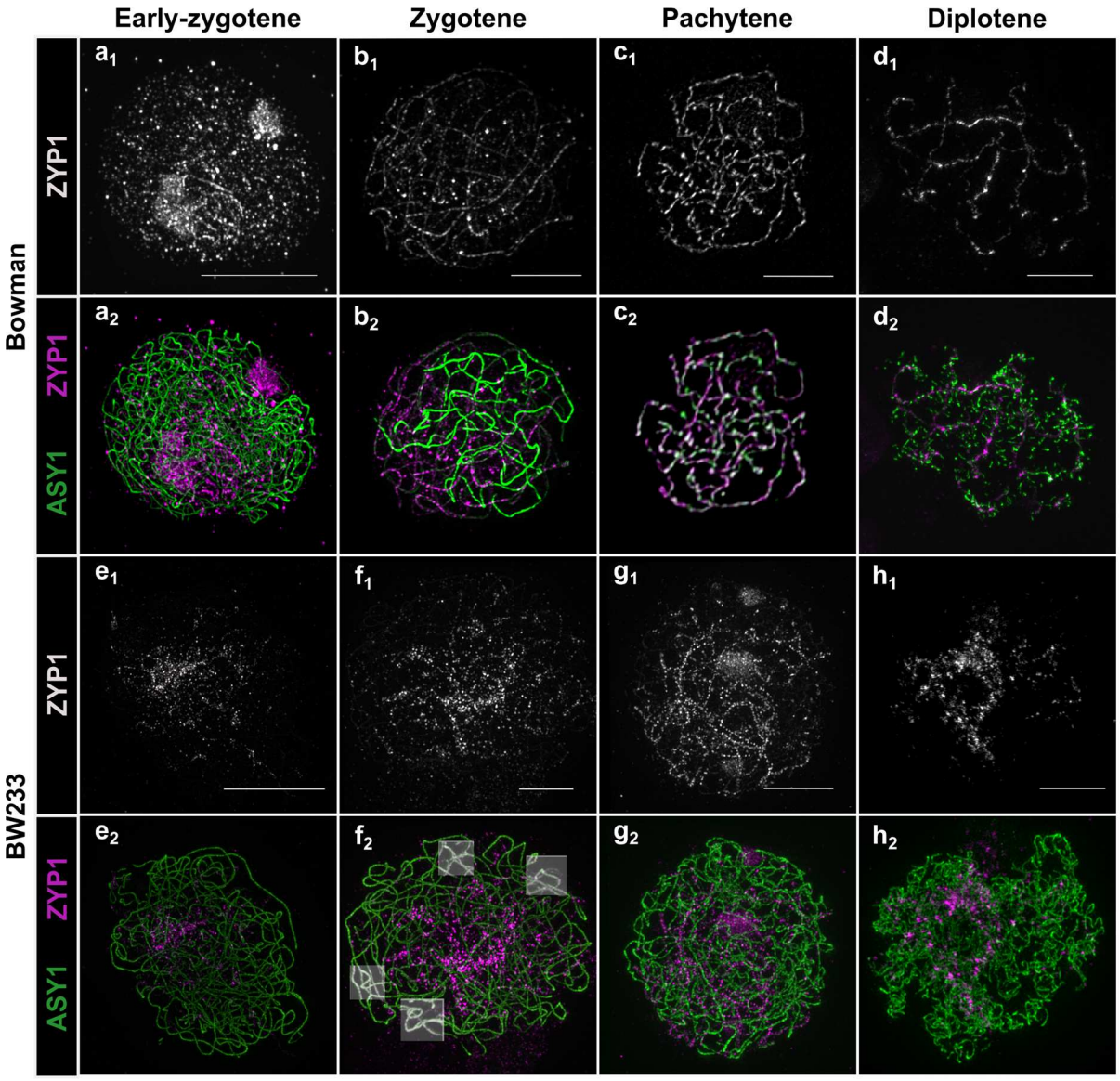

391

Figure 3: Synapsis

(a-d) Normal synapsis progression in Bowman. a) ZYP1 polymerization starts at one side of the nucleus and elongates during b) zygotene stage. Homologous chromosomes are fully aligned *via* ZYP1 at c) pachytene and get separated at d) diplotene exhibiting normal tinsel chromosomes. e) Somewhat normal initiation of synapsis in BW233. f) zygotene cells of BW233 show abnormal elongation of the ZYP1 "cluster" and unresolved interlocks (highlighted boxes). g) BW233 pachytene-like cell showing persistent HvZYP1 "clustering". h) BW233 diplotene cells exhibiting abnormal tinsel chromosomes. (a-h) ASY1: green, ZYP1: grey or magenta, scale bars 5 µm.

We found that *Hvst1* mutants had a large number of chromosomal interlocks compared to the WT (Fig. 3f_2, highlighted boxes) which could be the result of the synapsis delay or abnormal telomere organization. Therefore, we looked at telomere dynamics alongside synapsis and, in both genotypes, the telomeres cluster to one side of the nucleus (Fig.4a, d), suggesting that telomere clustering is not compromised in the mutant. As synapsis progresses, the telomeres move around the nuclear envelope in the WT (Fig. 4b, c) but retain some polarization in *Hvst1* (Fig. 4e, f) indicating that compromised ZYP1 elongation and/or the presence of multiple interlocks affects their movement. The absence of HvST1 function does not therefore compromise initial chromosome alignment but does compromise both progression and dissolution of synapsis.

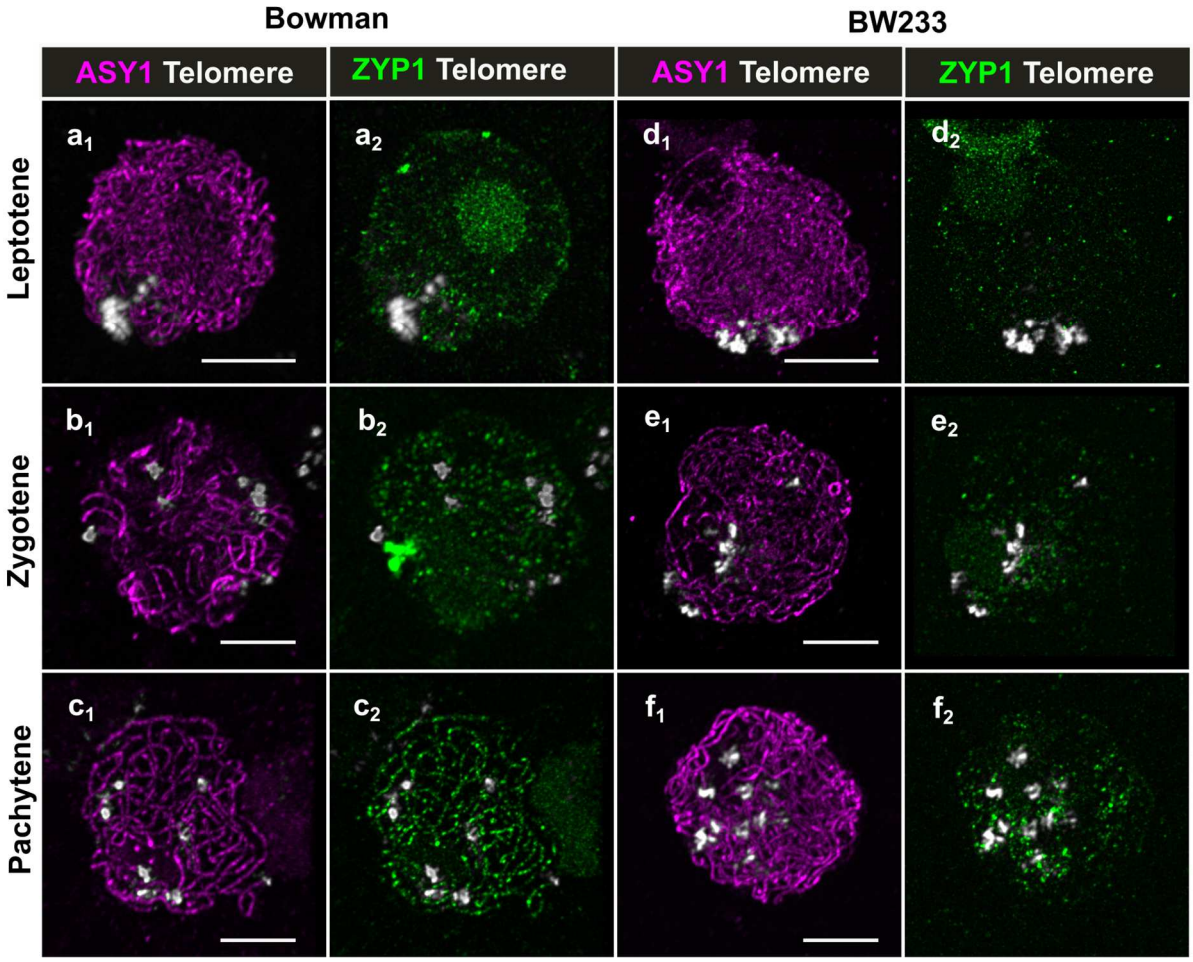

Figure 4. Telomere organization in WT and *Hvst1*

At leptotene stage, telomeres (grey) cluster at one side of the nucleus in both a) Bowman and d) BW233. As synapsis progresses from b) zygotene to c) pachytene stage, telomeres start to move around the nuclear periphery in Bowman. However, in BW233 e) zygotene and f) pachytene-like stage cells, they are still located at one side of the nucleus. Scale bar 5 µm

We followed synapsis progression and telomere movement using antibodies against ZYP1 and H3K27me3 respectively (Fig.5). At early-zygotene, ZYP1 starts to polymerize in both WT and BW233 and H3K37me3 signals are diffuse (Fig.5a, b). At pachytene, H3K27me3 forms a clear pattern in the WT as described in Baker *et al.* (2015) (Fig. 5e), but not in BW233 where H3K27me3 remains diffuse (Fig. 5d) suggesting a potential change in chromatin state in the mutant. To confirm this, we profiled histone methylation in anthers at pre-meiosis, leptotene/zygotene, pachytene/diplotene and a non-meiotic sample (root). We identified histones H1, H2.A, H2.B, H3, H3 centromeric, and H4 in all samples as well as methylation in H2A, H2B, H3 and H4 (Fig. S15, Table S6). No significant quantitative difference in histone methylation (Kruskal-Wallis test, Benjamini Hochberg correction) was observed (Fig. S15) between WT Bowman and BW233.

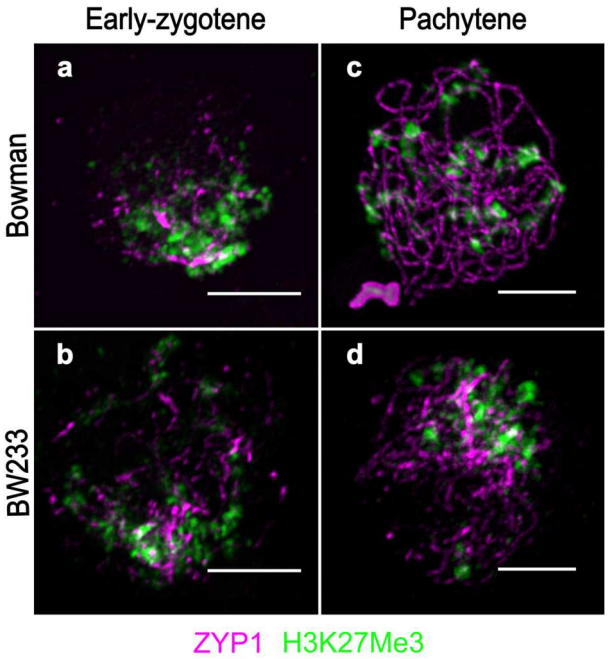

Figure 5. Chromatin behaviour and histone methylation in Bowman and BW233

At the beginning of ZYP1 (magenta) polymerization chromatin seems loose as shown by the diffuse H3K27me3 (green) around the telomere region in both a) Bowman and b) BW233. c) in Bowman at pachytene, the H3K27me3 signal is orderly allowing identification the telomeric regions. d) In BW233, the H3K27me3 signal is more diffuse as a result of abnormal synapsis. Scale bar 5um.

416 **Recombination is increased in *Hvst1* mutant progeny**

417 To understand the effect of *Hvst1* on recombinaiton we first used antibodies raised against early and
418 late recombination markers. Co-immunolocalisation of HvDMC1 (early recombination) and HvASY1
419 (chromosomes axes) in both WT and mutant (Colas *et al.,* 2019) showed that HvDMC1 behaviour was
420 similar in both genotypes at the beginning of synapsis (Fig. 6a, 6e) but that HvDMC1 foci persist in the
421 mutant compared to the WT (Fig. 6e) at later stages. However, DMC1 foci counts did not show a
422 significant difference at the leptotene-zygotene transition or at zygotene (Fig. 6i; Student's T-test,
423 p=0.31 and 0.58), suggesting that HvST1 is not involved in the recruitment of HvDMC1. However, the
424 persistance of foci at later stages is indicative of the delay in synapsis. Co-immunolocalisation of MLH3
425 (late recombination) and ZYP1 (chromosomes axes) in both WT and *Hvst1* was difficult to conduct due
426 to abnornal synapsis in the mutant. Given the inability to accurately stage late prophase I in BW233
427 meiocytes due to the perturbation of SC dissolution we compared anthers of similar size as anther size
428 is strongly correlated with meiotic progression (Arrieta *et al.,* 2020). We found that for similarly sized
429 anthers, WT Bowman displayed resolved MLH3 foci at pachytene while BW233 did not (Fig. S16),
430 which is consistent with a delay in crossover resolution (Colas *et al.,* 2016). Co-immunolocalisation of
431 MLH1 (Fig. S17) revealed a similar pattern to MLH3, with a large number of intermediates which persist
432 at later stages. These intermediates converge into larger stretches as prophase I progresses but fail to
433 resolve as discrete foci (Fig. S7f). The class I crossover resolution marker HEI10 (Ziolkowski *et al.*,
434 2017; Serra *et al.,* 2018) typically loads on chromosome axes at zygotene (Fig. 6b) and co-localises
435 with ZYP1 at pachytene (Fig. 6d) in WT Bowman. In BW233, although HEI10 maintains co-localisation
436 with ZYP1, it does not form typical distinct foci but co-localises with the abnormal ZYP1 polycomplex-
437 like structure (Fig. 6f, h).

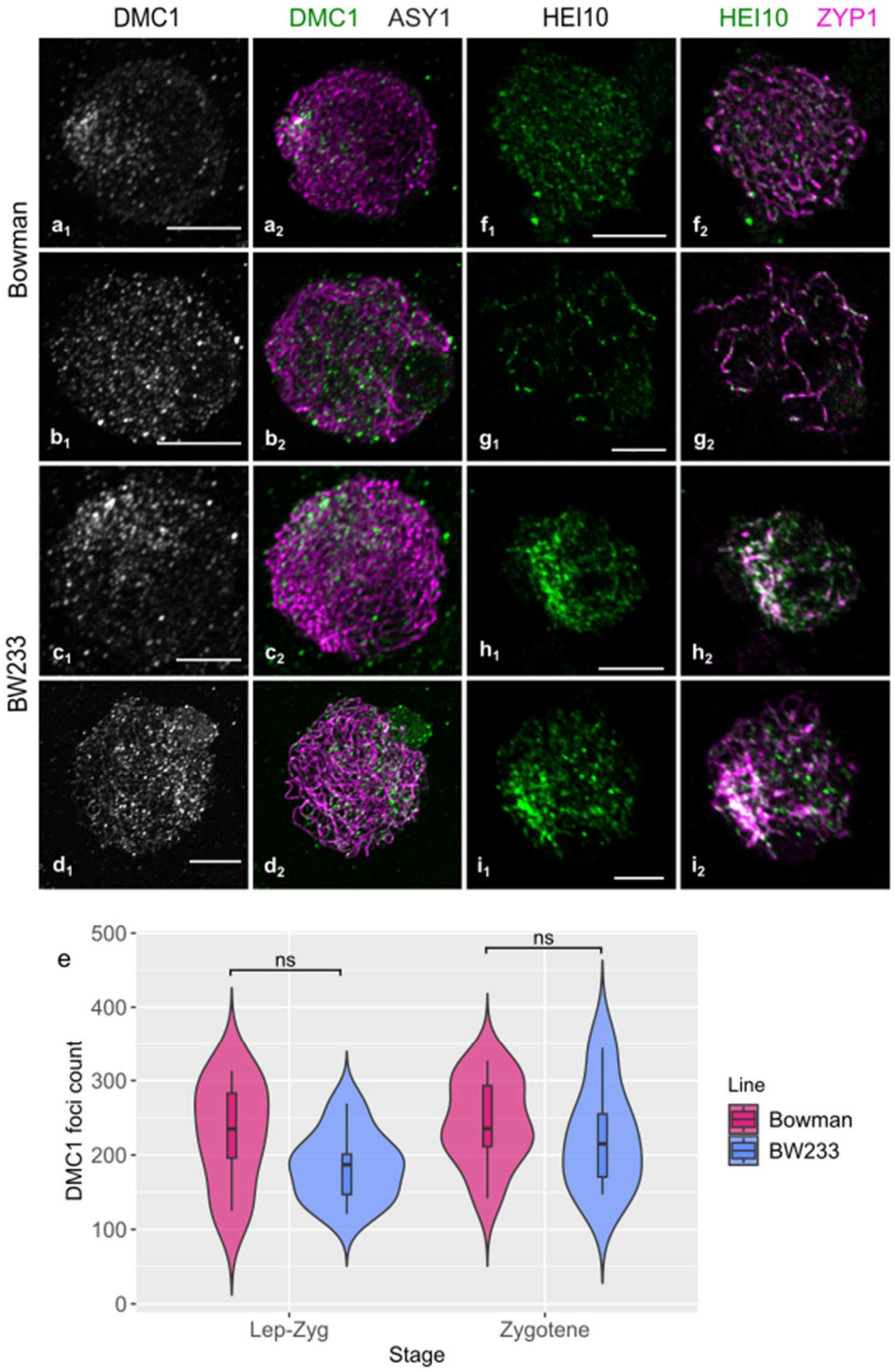

Figure 6: DMC1 and Hei10 distribution

At leptotene stage, DMC1 foci (green, grey) cluster at one side of the nucleus in a) Bowman and disperse along the ASY1 axes (Magenta) during b) zygotene. In BW233, we see the same behaviour at c) leptotene and d) zygotene. e) Violin plot of DMC1 foci count showing no significant difference between Bowman and BW233. HEI10 foci load on ZYP1 axes in both f,g) Bowman and h,i) BW233, but they resolve as large foci in g) bowman pachytene cells while they cluster around the ZYP1 polycomplex in h,i) BW233. scale bar 5µm

440 Due to the stickiness of *Hvst1* chromosomes, the unclear MLH3 labelling and the HEI10 polycomplex,
441 it was not possible to obtain accurate chiasma or MLH3/HEI10 foci counts from immunocytology of
442 meiocytes. We therefore directly assessed recombination in *Hvst1* mutant progeny by genetic analysis
443 of 400 F_3 plants derived from 24 F_2 families selected from a cross between BW233 (*Hvst1*) x cv. Barke
444 (*HvST1*) after using Marker Assisted Selection (MAS) to identify genotypes homozygous for *HvST1* or
445 *Hvst1.* We focused initially on chromosomes 1H, 5H, and 6H using 48 KASPar markers (LGC
446 Genomics). We observed that despite indicative observations in metaphase I meiotcytes the result of
447 *Hvst1* mutation was a significant increase in distal recombination events in *Hvst1* compared to the WT
448 F3 families for all three chromosomes. To confirm that increased recombination in *Hvst1* was genome-
449 wide, we then chose 95 of the 400 F_3 plants and genotyped them using the barley 50K iSelect SNP
450 array (Bayer *et al.,* 2017). We calculated genome wide recombination frequency after filtering for poorly
451 mapped markers and F_2 recombination events (Fig. S18). Total observed crossovers increased in *Hvst1*
452 compared to *HvST1* across all chromosomes—primarily distally—by an average of 76% and up to 149%
453 (Fig. 7; Table S7). This shows that the absence of HvST1 E3 ligase activity increased meiotic
454 recombination in those meiocytes which formed viable gametes.

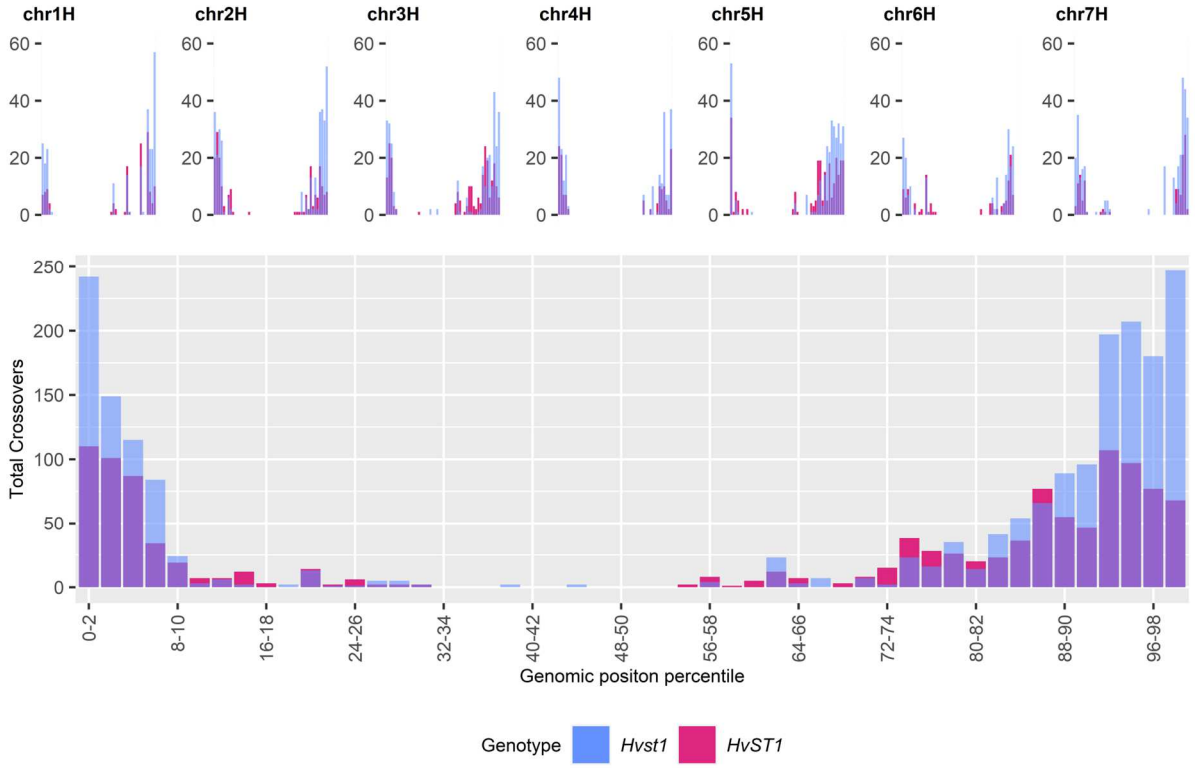

455

Figure 7: Recombination

Comparison of the total number of crossover events detected using 50K iSelect markers across all seven chromosomes (represented individually above and combined below) between *Hvst1* (in Blue; n=95) and *HvST1* (WT; in pink; n=95) per binned (2%) genomic position (Mbp) percentile.

456

457 **HvST1 is capable of ubiquitinating ASY1**

458 To determine if abnormal synapsis observed in *Hvst1* mutants might be explained by failure of SC
459 protein ubiquitination (required for their removal by the proteasome), we conducted an *in vitro* substrate
460 ubiquitination assay with purified HvASY1 and HvST1 proteins. We found that HvASY1 is ubiquitinated
461 in the presence of HvST1 and all other required components of the ubiquitination cascade (Fig. 8a),
462 visible as an increase in mass on western blots probed using anti-ASY1 antibody. No high molecular
463 weight protein is labelled in anti-ASY1 western blots in the absence ATP, with purified Hvst1, or in the
464 absence of HvASY1 (Fig. 8a) suggesting that the observed ubiquitination of HvASY1 is dependent on
465 the HvST1 RING domain and the ubiquitination cascade. To confirm that high molecular weight HvASY1
466 was ubiquitinated, the polyubiquitinated products of this assay were captured using GST-TUBE and
467 treated with broad spectrum deubiquitinating enzyme which recovered HvASY1 at its original mass (Fig.
468 8b).

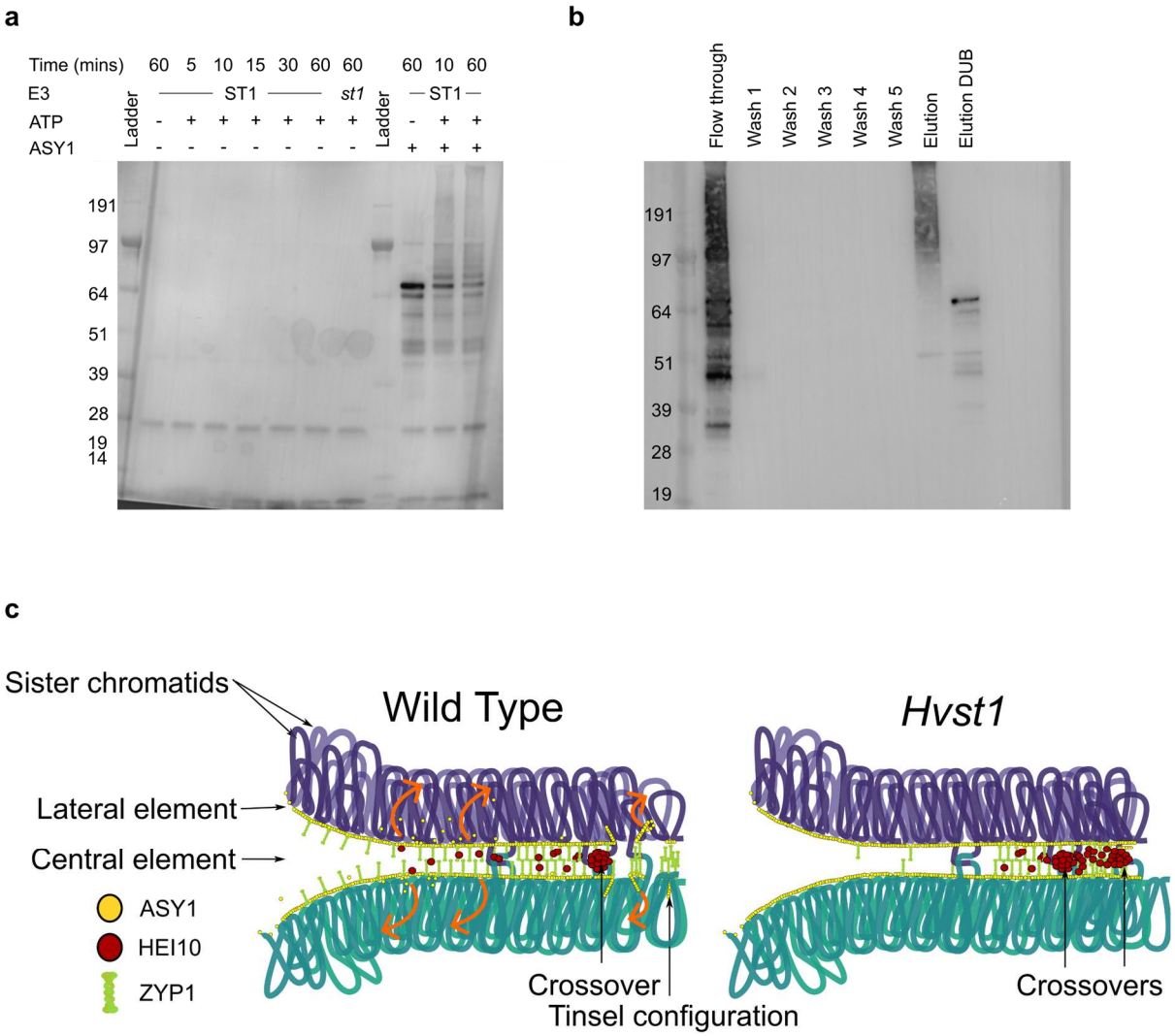
a
Time (mins)
60 5 10 15 30 60 60 60 10 60
E3
ST1
st1
ST1
ATP
ASY1
Ladder
Ladder
191
97
64
51
39
28
19
14
b
Flow through
Wash 1
Wash 2
Wash 3
Wash 4
Wash 5
Elution
Elution DUB
191
97
64
51
39
28
19
c
Sister chromatids
Wild Type
Hvst1
Lateral element
Central element
ASY1
HEI10
ZYP1
Crossover
Tinsel configuration
Crossovers

469

Figure 8. Ubiquitination of ASY1 by HvST1

a) Anti-ASY1 western blot of HvST1 autoubiquitination time course and HvST1-ASY1 substrate ubiquitination assay; lane description from left: 1-ladder; 2-HvST1 autoubiquitination no ATP control, 3-7: HvST1 autoubiquitination time course, 8: Hvst1 autoubiquitination control, 9: ladder, 10: HvST1-ASY1 substrate ubiquitination no ATP control, 11-12: HvST1-ASY1 substrate ubiquitination assay. b) Western blot of fractions recovered from GST-TUBE capture of polyubiquitinated products of HvST1-HvASY1 substrate ubiquitination assay probed with anti-HvASY1 antibody. HvASY1 antibody labels TUBE captured ubiquitinated protein in the eluted fraction and upon treatment of this fraction with broad spectrum deubiquitinating (DUB) enzyme ASY1 is returned to its original size (~64 KDa). Marker sizes in KDa are indicated on the left. c) proposed model of the role of HvST1 in synapsis (purple loops= homologue 1; sea green loops=homologue 2. In the wild type, synapsis is synchronized and ZYP1 polymerises between the two homologues dependent on continuous ASY1 turnover while the pro-crossover factor HEI10 diffuses along the ZYP1 axes. In *Hvst1* mutants, ASY1 turnover is compromised leading to partial synapsis and formation of the ZYP1 cluster while diffusion of HEI10 is constrained to partially synapsed regions, affecting coarsening dynamics by increasing the subtelomeric concentration of HEI10, leading to more crossovers which are closer together in this region.

Discussion

In plants, mammals, and budding yeast the formation of crossovers and synapsis are tightly linked (Grey *et al.,* 2022). We have previously shown that mutations in barley meiotic genes dramatically affect meiosis and, in general, reduce recombination (Colas *et al.,* 2016: Colas *et al.,* 2019) but also that mutations in conserved meiotic genes in barley (Colas *et al.,* 2016; Colas *et al.,* 2023) do not always lead to the expected phenotype when compared to other plants, including *Arabidopsis* (Jackson *et al.,* 2006; Bleuyard *et al.,* 2004) or rice (Ren *et al.,* 2021).

Here, we have identified and characterized an E3 ubiquitin ligase that is highly expressed during meiosis, providing the first evidence of a unique ubiquitination pathway that regulates meiosis in barley. We have called this gene *HvST1* (Sticky Telomeres 1), due to the stickiness of chromosomes at metaphase I that seemed to be in the telomere region. This stickiness made chiasma counts in *Hvst1* challenging but we did find a significant increase in the average number rod bivalent chromosomes and decrease in ring bivalent chromosomes were observed in *Hvst1* metaphase compared to the WT. We also observed a large variation in chiasma number in BW233 compared to the WT which in return led to a significant, albeit small, decrease of chiasma in BW233 compared to the WT, reflecting different metaphase configurations.

The most significant phenotype of the *Hvst1* genotype was abnormal synapsis due to the formation of ZYP1 polycomplex-like “clusters” near the telomere region. Contrary to our initial hypothesis, we found that initial formation of the telomere cluster was not altered in the mutant but that the telomeres tended to remain located at one side of the nucleus alongside ZYP1 clustering at the onset of delayed synapsis. Moreover, analysis of the chromatin state in BW233 using antibodies targeting methylated histones indicated altered chromatin state, although proteomic analysis of histone methylation did not show statistically significant differences in any such modification. This suggests that HvST1 activity does not

494 regulate the relative amount of histone methylation although it is still possible that loss of HvST1 function
495 may affect the distribution of histone methylation along the chromatin length. Accordingly, the apparent
496 reduction of chromatin compaction in BW233 is likely a reflection of delayed synapsis.

497 We also found that altered distribution of ZYP1 in *Hvst1* constrained the distribution of HEI10 in late
498 prophase, while HvDMC1 and MLH3 recruitment was unaltered, but failed to resolve into discrete foci.
499 The failure of MLH3 foci formation and concentration of HEI10 in the sub telomeric polycomplex also
500 prohibited cytological counting of class I crossovers based on recombination intermediate foci in late
501 prophase I. However, F3 50K genetic recombination data showed a clear and substantial increase in
502 the number of sub-telomeric recombination events in *Hvst1* relative to the WT. Further work is required
503 to determine the pathway responsible for this increase in recombination. Successful progeny included
504 in the genetic recombination data likely represent a bias towards less extreme male meiotic phenotypes
505 exhibiting better chromosome alignment (Fig. S9) and proper segregation as these are more likely to
506 develop to form fertile pollen. As such, the genetic recombination data, while a direct reflection of the
507 effective recombination rate between generations, is an incomplete representation of cytological CO
508 repair pathways. An increase in recombination alongside a higher number of rod bivalent chromosomes
509 at metaphase can be explained by a loss of obligate crossovers alongside crossovers which occur
510 closer together which can be counted as a single chiasma as reported in the wheat *fancm* mutant
511 Desjardins *et al.,* 2022) and the *Arabidopsis zyp1* mutants (France *et al.,* 2021). The phenotype of *Hvst1*
512 bears some other similarities to *zyp1* null mutants in *Arabidopsis* including persistent chromosome
513 interlocks and failure of ASY1 depletion (Capilla-Perez *et al.,* 2021; France *et al.,* 2021). This indicates
514 that much of the *HvST1* phenotype might derive from downstream effects of the failure or severe delay
515 in complete ZYP1 polymerization.

516 Polyubiquitination of HvASY1 by HvST1 but not Hvst1 *in vitro* provides an indication that the lack of
517 ZYP1 polymerization observed in *Hvst1* may result from the loss of this post translational modification
518 of ASY1. This observation supports the findings of Osman, *et al*. (2018) who previously identified
519 proteasomal and ubiquitination related proteins in association with ASY1 in a pulldown from *Brassica*
520 *oleracea* and is consistent with the observed localisation of ubiquitination to the chromosomal axes
521 during meiotic prophase (Rao *et al.,* 2017; Orr *et al.,* 2021b). RING type E3 ubiquitin ligases confer
522 specificity to the ubiquitination cascade by binding both E2-conjugating enzymes, thereby increasing
523 the reactivity of E2-Ub conjugates, and substrate proteins, catalysing the direct transfer of ubiquitin to
524 the substrate protein itself, or existing polyubiquitin chains on its surface (Dove *et al.,* 2016; Iconomou
525 and Saunders, 2016). The requirement for a functional RING domain for HvST1-HvASY1 interaction is
526 evident in the lack of ASY1 ubiquitination in the absence of the E2 interacting RING domain in Hvst1
527 (Fig. 8a). The canonical fate of polyubiquitinated proteins is proteasomal degradation, although a range
528 of substrate fates can arise from ubiquitination determined by polyubiquitin chain topology, which is
529 itself largely driven by a preference for particular lysine residues on the part of the interacting E2s (Dove
530 *et al.,* 2016). Combining this observation with the observed retention of ASY1 on the axis in late
531 prophase I in BW233 (Fig. 3g-h), peak of *HvST1* expression in meiocytes at Pachytene-Diplotene (Fig

532 2b), the co-localisation of pro-crossover factor HEI10 with ZYP1 during delayed BW233 ZYP1
533 polymerisation (Fig. 6f, 6h), and the significant increase in distal recombination events in homozygous
534 *Hvst1* progeny in both KASP and iSelect 50K analysis (Fig. 7), we propose a model for HvST1 function
535 in barley meiosis (Fig 8c) in which ASY1 turnover in early prophase I is required for ZYP1 polymerisation
536 and by extension for normal SC formation, crossover resolution, and interference. A requirement for
537 lateral element ubiquitination and proteasomal degradation for synapsis progression has been
538 previously demonstrated in mice where interaction of the SKP1-Cullin-F-box (SCF) complex in
539 conjunction with F-box protein FBXO47 with ASY1 orthologue HORMAD1 is required for normal
540 progression of synapsis (Guan *et al.,* 2022; Ma *et al.,* 2024).

541 In *Hvst1* mutants HEI10 distribution is clearly constrained by altered ZYP1 distribution resulting in a
542 localised increase in HEI10 concentration and long stretches of HEI10 in partially synapsed regions as
543 opposed to discrete foci. It has been demonstrated that the distribution of HEI10 is constrained by
544 ZYP1—so long as ZYP1 is present—and that altered ZYP1 distribution can affect crossover number
545 and distribution (Capilla-Perez *et al.,* 2021; France *et al.,* 2021; Fozard *et al.,* 2023). In this context, the
546 observed increase in distal recombination in *Hvst1* may be best understood within the proposed HEI10
547 coarsening model (Morgan *et al.,* 2021). It has been demonstrated that an increase in HEI10
548 concentration results in a reduction in crossover interference and an increase in the total number of
549 crossovers (Ziolkowski *et al.,* 2017). The HEI10 coarsening model proposes that class I crossover
550 number and distribution can largely be attributed to the concentration, SC restricted diffusion, and
551 reduced rate of escape over time of HEI10 from larger foci at recombination intermediates which are
552 then resolved as crossovers. However, altered synapsis in *Hvst1* mutants prohibited accurate
553 cytological counting of class I or class II recombination intermediates (Fig. 6, S16, S17), putting
554 determination of the crossover pathway responsible for the increase of recombination observed in
555 KASP marker and 50K recombination analysis outside the scope of this work.

556 Recent description of the rice *Osclr1*/*dsnp1* meiotic phenotype highlights several similar
557 immunocytological observations, including the formation of a ZEP1 polycomplex, the ZYP1 equivalent
558 in rice, and failure of PAIR2 depletion, the ASY1 equivalent in rice, indicating conserved meiotic function
559 in grasses (Ren *et al.,* 2021). However, the induced *dsnp1* mutation rendered these plants completely
560 sterile, *Osdsnp1* metaphase spreads do not show the lack of chromosome condensation observed in
561 *Hvst1,* and the ZEP1 polycomplex does not appear to retain subtelomeric localization as in *Hvst1* (Ren
562 *et al., .* 2021). The authors also reported reduction in class I crossovers based on reduced chiasmata
563 counts in *Osdsnp1* compared to the WT and decreased HEI10 foci counts in a *Osdsnp1/zep1* double
564 mutant background when compared to both the WT and *zep1* single mutant (Ren *et al.,* 2021). The
565 induced mutation in *Osdsnp1* is highly similar to *Hvst1* occurring early in the RING domain and
566 presumably resulting in loss of E3 ligase activity (Ren *et al.,* 2021). Although OsDSNP1/OsCLR1 has a
567 reported gain of function in response to heat and drought stress which is not conserved in other grasses
568 (Park *et al*., 2019), indicating some evolutionary divergence, it does not seem likely that the function of
569 this protein is meaningfully divergent from HvST1 in meiosis. The reported reduction in *Osdsnp1*

570 chiasma may reflect the greater proximity of crossovers we observe in genetic recombination data,
571 resulting in inaccurate counts as described by Desjardins *et al.* (2022). The slight reduction of HEI10
572 foci in the *Osdsnp1/zep1* double mutant background compared to the WT might indicate that the
573 increase in recombination we observe in *Hvst1* is due to class II crossover resolution, or that the altered
574 ZYP1 environment and partial synapsis is essential to the increase in recombination observed in *Hvst1*.
575 The comparatively large reduction in HEI10 foci in *Osdsnp1/zep1* compared to the *zep1* single mutant
576 is intriguing, possibly indicating a role for HvST1 in regulating class I crossover resolution beyond its
577 impact on ZYP1 polymerization, whether through ASY1 ubiquitination or of other targets. Complete
578 sterility and the distinct ZEP1 polycomplex behaviour in *Osdsnp1* most likely reflect fundamental
579 differences in genome size, chromatin organization, and timing during meiosis between rice and barley.
580 Further work is required to identify and validate the targets of HvST1 E3 ligase activity *in vivo* and to
581 elucidate the protein-protein interactions underlying the *Hvst1* meiotic phenotype.

582 There is increasing interest in methods of altering the recombination landscape in plants through
583 targeting of post-translational modifications and the use of methods such as virus induced gene
584 silencing (VIGS) to downregulate crossover suppressive genes in order to reduce the time, resources,
585 and emissions associated with generating novel crop varieties with desirable traits (Desjardins *et al.,*
586 2020. Raz *et al.,* 2020). Further investigation of the molecular mechanics of *HvST1* might reveal new
587 pathways and additional targets for such approaches. Similarly, identifying alternative mutations in
588 *HvST1*, its promoter, targets, or proteins regulating its activity might result in a similar increase in
589 recombination without the same degree of semi sterility which would enhance its use in plant breeding.
590 While it is presently unclear exactly how subtelomeric recombination is increased in *Hvst1,* this mutation
591 could find immediate practical application in breeding programs to increase recombination—in
592 particular, between chromosomes of distantly related genotypes that are being exploited as a source
593 of novel traits such as disease, heat, and drought resistance and to disrupt stubborn linkage drag. Serra
594 *et al.* (2018) demonstrated that combining *HEI10* overexpression with mutation of *recq4*, an inhibitor of
595 class II COs, led to an additive increase in recombination in Arabidopsis. Combining *Hvst1* with the
596 recently described *Hvrecql4* mutation (Arrieta *et al.,* 2021) may also lead to such an additive effect and
597 may provide further insight into the pathway leading to the observed increase in recombination in *Hvst1*.

598

599 **Acknowledgments**

600 The authors would like to thank Prof. Ron Hay, Dr Federico Pelish, and Dr Frank Wright for providing
601 advice on the experiments and Dr Michael Skelly for providing the GST-TUBE construct. This research
602 was funded by Biological Science Research Council Grant BB/T008636/1, with support data generated
603 under the European Community's Seventh Framework Programme *FP7/2007-2013 (n°* 222883), the
604 European Research Council Grant Shuffle (Project ID: 669182), and the Scottish Government's Rural
605 and Environment Science and Analytical Services Division work programme Theme 2 WP2.1 RD1 and
606 RD2. OMX microscopy was supported by the Euro-BioImaging PCS to I.C. and through the MRC Next
607 Generation Optical Microscopy Award (Ref: MR/K015869/1) at the CAST Facility, University of Dundee.

608 All other microscopy work was supported by the Imaging Facility of the James Hutton Institute. SM was
609 supported by the joint James Hutton Studentship program and EASTBIO fellowship (2013-2017).
610 pDEST-HisMBP was a gift from David Waugh (Addgene plasmid #11085).

611 **Competing Interest Statement:** The authors declare no competing interests.

612 **Author Contributions:** IC, LR, JO, SM and RW designed the experiment. SM, JO, DL, MM, AB, and
613 NM conducted the experiments and data analyses. JO, RW, and IC wrote the manuscript. All authors
614 reviewed the manuscript.

615 **Data availability:** Barley 50K iSelect recombination data is available on FigShare
616 (https://doi.org/10.6084/m9.figshare.21427953.v1). Raw immunocytology images are available from
617 the corresponding author upon reasonable request.

618 **Code availability:** Code used in data analysis and plotting for this study is available at
619 https://github.com/BioJNO/HvST1.

620

621 ## References

622 **Altschul SF, Gish W, Miller W, Myers EW, Lipman DJ. 1990.** Basic local alignment search tool. J
623 Mol Biol. **215**(3):403-10.
624
625 **Arrieta M, Macaulay M, Colas I, Schreiber M, Shaw PD, Waugh R, Ramsay L. 2021.** An Induced
626 Mutation in *HvRECQL4* Increases the Overall Recombination and Restores Fertility in a Barley
627 *HvMLH3* Mutant Background. Front Plant Sci.**12**:706560.
628
629 **Arrieta M, Colas I, Macaulay M, Waugh R, Ramsay L. 2020.** A Modular Tray Growth System for
630 Barley. in Plant Meiosis: Methods and Protocols, M. Pradillo, S. Heckmann, Eds. (Springer New York,
631 New York, NY, 2020), 10.1007/978-1-4939-9818-0_26, pp. 367-379.
632
633 **Baker K, Dhillon T, Colas I, Cook N, Milne I, Milne L, Bayer M, Flavell AJ. 2015.** Chromatin state
634 analysis of the barley epigenome reveals a higher-order structure defined by H3K27me1 and
635 H3K27me3 abundance. The Plant Journal. **84**. 111-124
636
637 **Barakate A, Orr J, Schreiber M, Colas I, Lewandowska D, McCallum N, Macaulay M, Morris J,**
638 **Arrieta M, Hedley PE, Ramsay L, Waugh R. 2021**. Barley Anther and Meiocyte Transcriptome
639 Dynamics in Meiotic Prophase I. Front Plant Sci. **11**:619404.
640
641 **Bartlett JG, Alves SC, Smedley M, Snape JW, Harwood WA. 2008.** High-throughput
642 Agrobacterium-mediated barley transformation. Plant Methods**. 4**:22.

643
644 **Bayer MM, Rapazote-Flores P, Ganal M, Hedley PE, Macauley M, Plieske J, Ramsay L, Russell**
645 **J, Shaw PD, Thomas W, Waugh R. 2017.** Development and Evaluation of a Barley 50k iSelect SNP
646 Array. Frontiers in Plant Science. **8** (1792).
647
648 **Bleuyard JY, White CI. 2004.** The Arabidopsis homologue of Xrcc3 plays an essential role in
649 meiosis. EMBO J. **23**(2):439-49.
650
651 **Bolser D, Staines DM, Pritchard E, Kersey P. 2016.** Ensembl Plants: Integrating Tools for
652 Visualizing, Mining, and Analyzing Plant Genomics Data. Methods Mol Biol. **1374**:115-40.
653
654 **Capilla-Pérez L, Durand S, Hurel A, Lian Q, Chambon A, Taochy C, Solier V, Grelon M, Mercier**
655 **R. 2021.** The synaptonemal complex imposes crossover interference and heterochiasmy in
656 *Arabidopsis*. Proc Natl Acad Sci U S A. **118**(12):e2023613118.
657
658 **Close TJ, Bhat PR, Lonardi S, Wu Y, Rostoks N, Ramsay L, Druka A, Stein N, Svensson JT,**
659 **Wanamaker S, et al. 2009.** Development and implementation of high-throughput SNP genotyping in
660 barley. BMC Genomics. **10**:582.
661
662 **Colas I, Macaulay M, Higgins JD, Phillips D, Barakate A, Posch M, Armstrong SJ, Franklin FC,**
663 **Halpin C, Waugh R, Ramsay L. 2016.** A spontaneous mutation in MutL-Homolog 3 (HvMLH3) affects
664 synapsis and crossover resolution in the barley desynaptic mutant des10. New Phytologist.
665 **212**(3):693-707.
666
667 **Colas I, Darrier B, Arrieta M, Mittmann SU, Ramsay L, Sourdille P, Waugh R. 2017.** Observation
668 of Extensive Chromosome Axis Remodeling during the "Diffuse-Phase" of Meiosis in Large Genome
669 Cereals. Frontiers in plant science **8:**1235.
670
671 **Colas I, Barakate A, Macaulay M, Schreiber M, Stephens J, Vivera S, Halpin C, Waugh R,**
672 **Ramsay L. 2019.** *Desynaptic 5* carries a spontaneous semi-dominant mutation affecting Disrupted
673 Meiotic cDNA 1 in barley. Journal of Experimental Botany **70**(10):2683-2698.
674
675 **Colas I, Macaulay M, Arrieta M, Schreiber M, Orr JN, Sandhu A, Augustine A, Targońska-**
676 **Karasek M, Susan J Armstrong, Robbie Waugh, et al. 2023**. The *RAD51* paralogue *HvXRCC2*
677 regulates meiosis and recombination in barley. *bioRxiv.* doi:10.05.561044

678 **Colmsee C, Beier S, Himmelbach A, Schmutzer T, Stein N, Scholz U, Mascher M. 2015.** BARLEX
679 - the Barley Draft Genome Explorer. Mol Plant. **8**(6):964-6.
680

681 **Coulter M, Entizne JC, Guo W, Bayer M, Wonneberger R, Milne L, Schreiber M, Haaning A,**
682 **Muehlbauer GJ, McCallum N, et al. 2022.** BaRTv2: a highly resolved barley reference transcriptome
683 for accurate transcript-specific RNA-seq quantification. Plant J. **111**(4):1183-1202.
684
685 **Cox J, Mann M. 2008.** MaxQuant enables high peptide identification rates, individualized p.p.b.-range
686 mass accuracies and proteome-wide protein quantification. Nat Biotechnol. **26**(12):1367-72.
687
688 **Cox J, Neuhauser N, Michalski A, Scheltema RA, Olsen JV, Mann M. 2011.** Andromeda: a peptide
689 search engine integrated into the MaxQuant environment. J Proteome Res. **10**(4):1794-805.
690
691 **Da Ines O, Degroote F, Goubely C, Amiard S, Gallego ME, White CI. 2013**. Meiotic recombination
692 in Arabidopsis is catalysed by DMC1, with RAD51 playing a supporting role. PLoS Genet.
693 **9**(9):e1003787.
694
695 **Daoudal-Cotterell S, Gallego ME, White CI. 2002.** The plant Rad50-Mre11 protein complex. FEBS
696 Lett. **516**(1-3):164-6.
697
698 **De Muyt A, Mercier R, Mézard C, Grelon M. 2009**. Meiotic recombination and crossovers in plants.
699 Genome Dynamic **5**:14-25.
700
701 **Desjardins S, Kanyuka K, Higgins JD. 2020.** A Cytological Analysis of Wheat Meiosis Targeted by
702 Virus-Induced Gene Silencing (VIGS). Methods Mol Biol. **2061:**319-330.
703
704 **Desjardins SD, Simmonds J, Guterman I, Kanyuka K, Burridge AJ, Tock AJ, Sanchez-Moran E,**
705 **Franklin FCH, Henderson IR, Edwards KJ, et al. 2022.** FANCM promotes class I interfering
706 crossovers and suppresses class II non-interfering crossovers in wheat meiosis. Nat Commun.
707 **13**(1):3644.
708
709 **Dove KK, Stieglitz B, Duncan ED, Rittinger K, Klevit RE. 2016.** Molecular insights into RBR E3
710 ligase ubiquitin transfer mechanisms. EMBO Rep. **17**(8):1221-35.
711
712 **Druka A, Franckowiak J, Lundqvist U, Bonar N, Alexander J, Guzy-Wrobelska J, Ramsay L,**
713 **Druka I, Grant I, Macaulay M, et al. 2010.** Exploiting induced variation to dissect quantitative traits in
714 barley. Biochem Soc Trans. **38**(2):683-8.
715
716 **Druka A, Franckowiak J, Lundqvist U, Bonar N, Alexander J, Houston K, Radovic S, Shahinnia**
717 **F, Vendramin V, Morgante M, et al. 2011**. Genetic dissection of barley morphology and
718 development. Plant Physiol**. 155**(2):617-27.
719

720 **Emms DM, Kelly S. 2019.**OrthoFinder: phylogenetic orthology inference for comparative genomics.
721 Genome Biol. **20**(1):238.
722
723 **Falque M, Anderson LK, Stack SM, Gauthier F, Martin OC. 2009.**Two types of meiotic crossovers
724 coexist in maize. Plant Cell. **21**(12):3915-25.
725
726 **Fozard JA, Morgan C, Howard M. 2023.** Coarsening dynamics can explain meiotic crossover
727 patterning in both the presence and absence of the synaptonemal complex. eLife. **12**:e79408.
728
729 **France MG, Enderle J, Röhrig S, Puchta H, Franklin FCH, Higgins JD. 2021.** ZYP1 is required for
730 obligate cross-over formation and cross-over interference in *Arabidopsis*. Proc Natl Acad Sci U S A.
731 **118**(14):e2021671118.
732
733 **Grelon M, Vezon D, Gendrot G, Pelletier G. 2001.** AtSPO11-1 is necessary for efficient meiotic
734 recombination in plants. EMBO J. **20**(3):589-600.
735
736 **Grey C, de Massy B. 2022.** Coupling crossover and synaptonemal complex in meiosis. Genes Dev.
737 **36**(1-2):4-6
738
739 **Guan Y, Lin H, Leu NA, Ruthel G, Fuchs SY, Busino L, Luo M, Wang PJ. 2022.** SCF ubiquitin E3
740 ligase regulates DNA double-strand breaks in early meiotic recombination. Nucleic Acids Res**.**
741 **50**(9):5129-5144.
742
743 **Hartung F, Wurz-Wildersinn R, Fuchs J, Schubert I, Suer S, Puchta H. 2007.** The catalytically
744 active tyrosine residues of both SPO11-1 and SPO11-2 are required for meiotic double-strand break
745 induction in Arabidopsis. Plant Cell. **19**(10):3090-3099
746
747 **Hernandes-Soriano J.M. 1973.** Desynaptic mutants in betzes barley. (Master Thesis from The
748 University of Arizona).
749
750 **Higgins JD, Sanchez-Moran E, Armstrong SJ, Jones GH, Franklin FC. 2005.** The Arabidopsis
751 synaptonemal complex protein ZYP1 is required for chromosome synapsis and normal fidelity of
752 crossing over. Genes Dev. **19**(20):2488-500.
753
754 **Higgins JD, Buckling EF, Franklin FC, Jones GH. 2008a**. Expression and functional analysis of
755 AtMUS81 in Arabidopsis meiosis reveals a role in the second pathway of crossing-over. Plant J.
756 **54**(1):152-62.
757

758 **Higgins JD, Vignard J, Mercier R, Pugh AG, Franklin FC, Jones GH.2008b.** AtMSH5 partners
759 AtMSH4 in the class I meiotic crossover pathway in Arabidopsis thaliana, but is not required for
760 synapsis. Plant J. **55**(1):28-39.
761
762 **Higgins JD, Perry RM, Barakate A, Ramsay L, Waugh R, Halpin C, Armstrong SJ, Franklin FC.**
763 **2012.** Spatiotemporal asymmetry of the meiotic program underlies the predominantly distal
764 distribution of meiotic crossovers in barley. Plant Cell. **24**(10):4096-4109.
765
766 **Huerta-Cepas J, Szklarczyk D, Heller D, Hernández-Plaza A, Forslund SK, Cook H, Mende DR,**
767 **Letunic I, Rattei T, Jensen LJ, et al. 2019**. eggNOG 5.0: a hierarchical, functionally and
768 phylogenetically annotated orthology resource based on 5090 organisms and 2502 viruses. Nucleic
769 Acids Res. **47**(D1):D309-D314.
770
771 **Iconomou M, Saunders DN. 2016.** Systematic approaches to identify E3 ligase substrates. Biochem
772 J. **473**(22):4083-4101.
773
774 **Jackson N, Sanchez-Moran E, Buckling E, Armstrong SJ, Jones GH, Franklin FC.2006.** Reduced
775 meiotic crossovers and delayed prophase I progression in AtMLH3-deficient Arabidopsis. EMBO J.
776 **25**(6):1315-23.
777
778 **Katoh K, Misawa K, Kuma K, Miyata T. 2002**. MAFFT: a novel method for rapid multiple sequence
779 alignment based on fast Fourier transform. Nucleic Acids Res. **30**(14):3059-66.
780
781 **Künzel G, Waugh R. 2002.** Integration of microsatellite markers into the translocation-based physical
782 RFLP map of barley chromosome 3H. Theor Appl Genet. **105**(5):660-665.
783
784 **Lambing C, Heckmann S. 2018.** Tackling Plant Meiosis: From Model Research to Crop
785 Improvement. Front Plant Sci. **9**:829.
786
787 **Lewandowska D, Zhang R, Colas I, Uzrek N, Waugh R. 2019.** Application of a Sensitive and
788 Reproducible Label-Free Proteomic Approach to Explore the Proteome of Individual Meiotic-Phase
789 Barley Anthers. Front Plant Sci. **10**:393.
790
791 **Lundqvist U, Franckowiak J D, Konishi T. 1997.** New and revised descriptions of barley genes.
792 *Barley Genet. Newsl.* **26**, 22-516
793
794 **Ma A, Yang Y, Cao L, Chen L, Zhang JV. 2024.** FBXO47 regulates centromere pairing as key
795 component of centromeric SCF E3 ligase in mouse spermatocytes. Communications Biology. **7**
796 (1099).

Mascher M, Gundlach H, Himmelbach A, Beier S, Twardziok SO, Wicker T, Radchuk V, Dockter C, Hedley PE, Russell J, et al. 2017. A chromosome conformation capture ordered sequence of the barley genome. Nature. **544**(7651):427-433.

Mascher M, Wicker T, Jenkins J, Plott C, Lux T, Koh CS, Ens J, Gundlach H, Boston LB, Tulpová Z, et al. 2021. Long-read sequence assembly: a technical evaluation in barley. Plant Cell. **33**(6):1888-1906.

Mieulet D, Aubert G, Bres C, Klein A, Droc G, Vieille E, Rond-Coissieux C, Sanchez M, Dalmais M, Mauxion JP, et al. 2018. Unleashing meiotic crossovers in crops. Nat Plants. **4**(12):1010-1016.

Milne I, Shaw P, Stephen G, Bayer M, Cardle L, Thomas WT, Flavell AJ, Marshall D. 2010. Flapjack--graphical genotype visualization. Bioinformatics. **26**(24):3133-4.

Minh BQ, Schmidt HA, Chernomor O, Schrempf D, Woodhams MD, von Haeseler A, Lanfear R. 2020. IQ-TREE 2: New Models and Efficient Methods for Phylogenetic Inference in the Genomic Era. Mol Biol Evol. **37**(5):1530-1534.

Morgan C, Fozard JA, Hartley M, Henderson IR, Bomblies K, Howard, M. 2021. Diffusion-mediated HEI10 coarsening can explain meiotic crossover positioning in Arabidopsis. Nature Communications. **12** (4674).

Nallamsetty S, Austin BP, Penrose KJ, Waugh DS. (2009). Gateway vectors for the production of combinatorially-tagged His6-MBP fusion proteins in the cytoplasm and periplasm of Escherichia coli. Protein Science. **14**: 2964-2971.

Neale MJ, Keeney S. 2006. Clarifying the mechanics of DNA strand exchange in meiotic recombination. Nature. **442**(7099):153-8.

Orr JN, Lewandowska D, Waugh R, Colas I. 2021a. Chromosome Synapsis and Recombination in Cereals. *Annunal Plant Reviews Online* **4** (1). https://doi.org/10.1002/9781119312994.apr0710

Orr JN, Waugh R, Colas I. 2021b. Ubiquitination in Plant Meiosis: Recent Advances and High Throughput Methods. Front Plant Sci. **12**:667314.

Osman K, Yang J, Roitinger E, Lambing C, Heckmann S, Howell E, Cuacos M, Imre R, Dürnberger G, Mechtler K, et al. 2018. Affinity proteomics reveals extensive phosphorylation of the

835 Brassica chromosome axis protein ASY1 and a network of associated proteins at prophase I of
836 meiosis. Plant J. **93**(1):17-33.
837
838 **Park YC, Choi SY, Kim JH, Jang CS. 2019.** Molecular Functions of Rice Cytosol-Localized RING
839 Finger Protein 1 in Response to Salt and Drought and Comparative Analysis of Its Grass Orthologs.
840 Plant Cell Physiol. **60**(11):2394-2409.
841
842 **Phillips D, Nibau C, Wnetrzak J, Jenkins G. 2012.** High resolution analysis of meiotic chromosome
843 structure and behaviour in barley (Hordeum vulgare L.). PLoS One. **7**(6):e39539.
844
845 **Pradillo M, López E, Linacero R, Romero C, Cuñado N, Sánchez-Morán E, Santos JL. 2012.**
846 Together yes, but not coupled: new insights into the roles of RAD51 and DMC1 in plant meiotic
847 recombination. Plant J. **69**(6):921-33.
848
849 **Randall RS, Jourdain C, Nowicka A, Kaduchová K, Kubová M, Ayoub MA, Schubert V, Tatout**
850 **C, Colas I, Kalyanikrishna, et al. 2022.** Image analysis workflows to reveal the spatial organization
851 of cell nuclei and chromosomes. Nucleus. **13**(1):277-299.
852
853 **Rao HB, Qiao H, Bhatt SK, Bailey LR, Tran HD, Bourne SL, Qiu W, Deshpande A, Sharma AN,**
854 **Beebout CJ, et al. 2017.** A SUMO-ubiquitin relay recruits proteasomes to chromosome axes to
855 regulate meiotic recombination. Science. **355**(6323):403-407.
856
857 **Raz A, Dahan-Meir T, Melamed-Bessudo C, Leshkowitz D, Levy AA. 2021.** Redistribution of
858 Meiotic Crossovers Along Wheat Chromosomes by Virus-Induced Gene Silencing. Front Plant Sci.
859 **11**:635139
860
861 **Ren L, Zhao T, Zhao Y, Du G, Yang S, Mu N, Tang D, Shen Y, Li Y, Cheng Z. 2021.** The E3
862 ubiquitin ligase DESYNAPSIS1 regulates synapsis and recombination in rice meiosis. Cell Rep.
863 **37**(5):109941
864
865 **Serra H, Lambing C, Griffin CH, Topp SD, Nageswaran DC, Underwood CJ, Ziolkowski PA,**
866 **Séguéla-Arnaud M, Fernandes JB, Mercier R, et al. 2018.** Massive crossover elevation via
867 combination of *HEI10* and *recq4a recq4b* during *Arabidopsis* meiosis. Proc Natl Acad Sci U S A.
868 **115**(10):2437-2442.
869
870 **Skelly MJ, Furniss JJ, Grey H, Wong KW, Spoel SH. 2019.** Dynamic ubiquitination determines
871 transcriptional activity of the plant immune coactivator NPR1. Elife**. 8**:e47005.
872

Stam P. 1993. Construction of Integrated Genetic-Linkage Maps by Means of a New Computer Package - Joinmap. *Plant Journal* **3**, 739-744.

Stewart MD, Ritterhoff T, Klevit RE, Brzovic PS. 2016. E2 enzymes: more than just middle men. Cell Res. **26**(4):423-40.

Tyanova S, Temu T, Cox J. 2016. The MaxQuant computational platform for mass spectrometry-based shotgun proteomics. Nat Protoc. **11**(12):2301-2319.

Voorrips RE. 2002. MapChart: software for the graphical presentation of linkage maps and QTLs. J Hered. **93**(1):77-8.

Wang Q, Goldstein M, Alexander P, Wakeman TP, Sun T, Feng J, Lou Z, Kastan MB, Wang XF. 2014. Rad17 recruits the MRE11-RAD50-NBS1 complex to regulate the cellular response to DNA double-strand breaks. EMBO J. **33**(8):862-77.

Yu G. 2020. Using ggtree to Visualize Data on Tree-Like Structures. Curr Protoc Bioinformatics. **69**(1):e96.

Zickler D., Kleckner N. 2015. Recombination, Pairing, and Synapsis of Homologs during Meiosis. Cold Spring Harb Perspect Biol. 7(6):a016626.

Ziolkowski PA, Underwood CJ, Lambing C, Martinez-Garcia M, Lawrence EJ, Ziolkowska L, Griffin C, Choi K, Franklin FC, Martienssen RA, et al. 2017. Natural variation and dosage of the HEI10 meiotic E3 ligase control *Arabidopsis* crossover recombination. Genes Dev. **31**(3):306-317.

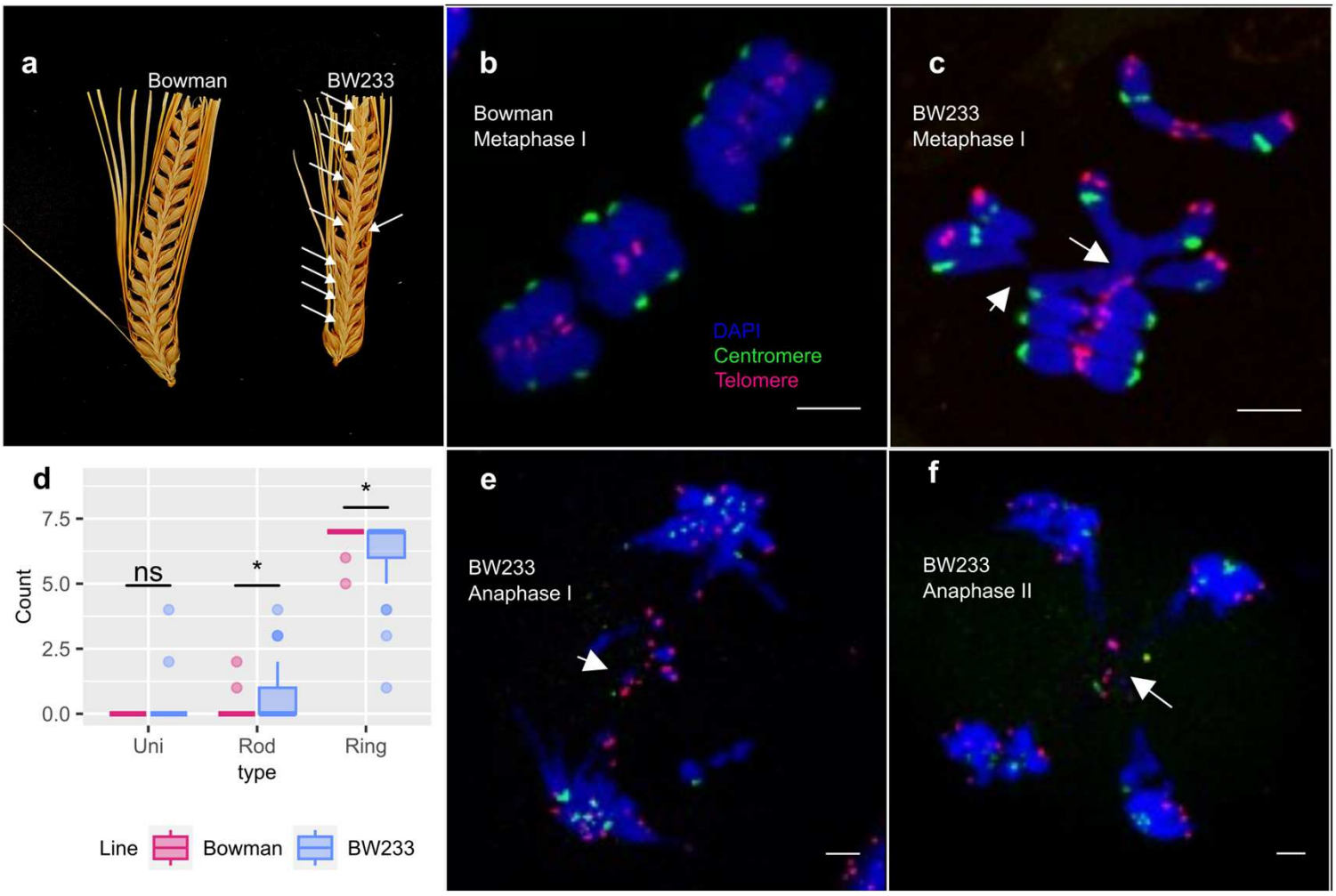

Figure 1: BW233 phenotype

a) Spike fertility comparison between Bowman and BW233, with missing seed indicated by white arrows. b) Bowman metaphase I with 7 ring bivalents. c) BW233 metaphase I, with 7 bivalents often interlocked at the telomere region (white arrows). d) Box plot of univalent, rod bivalent, and ring bivalent counts in *HvST1* and *Hvst1* plants with significance (T-test) indicated above. e) BW233 anaphase I, showing lagging chromosomes and chromosomes bridges (white arrow). f) BW233 anaphase II with interlocked chromosomes at the telomere region (white arrow). DAPI (blue), telomeres (red), centromeres (green). Scale bar 5 µm

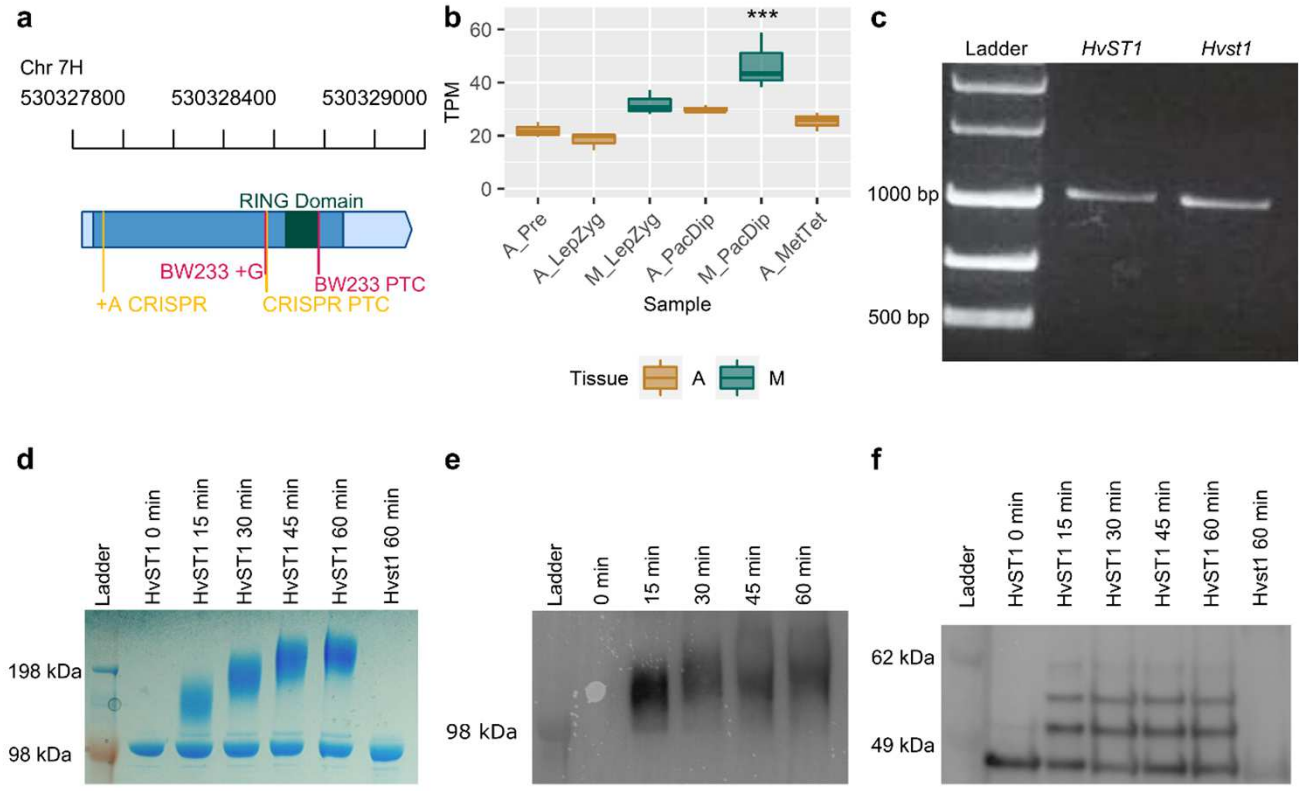

Figure 2: HvST1 characterisation

a) *HvST1* gene model derived from Barley Reference Transcriptome 2 (BaRT2v18; Coulter *et al.,* 2022) RNA sequences mapped to the barley cv Barke genome with the BW233 (*Hvst1)* insertion (+G) and premature termination codon (PTC) indicated in dark pink and the CRISPR/Cas9 insertion and PTC indicated in yellow. The region encoding the RING domain is indicated in dark green. WT 3′ and 5′ untranslated regions (UTRs) are indicated in light blue while WT coding sequences are indicated in dark blue. The physical genomic coordinates are indicated above. b) Expression profile of *HvST1* in time resolved anther and meiocyte expression data (Barakate *et al.,* 2021) where A=Anther, M=Meiocyte, Pre=pre-meiosis, LepZyg=Leptotene–Zygotene, PacDip=Pachytene–Diplotene, and MetTet=Metaphase–Tetrad. The statistical significance ($p<0.001$) of *HvST1* expression in meiocytes at Pachytene-Diplotene as determined by ANOVA and Tukey's honest significant difference is indicated above the box. c) agarose gel of FL cDNA from RT-PCR of *HvST1* from Bowman and *Hvst1* from BW233 anthers. d) Coomassie stained SDS-PAGE of autoubiquitination time-course assay. e) anti-ubiquitin conjugate probed western blot of HvST1 autoubiquitination time course assay. f) anti-HvST1 probed western blot of autoubiquitination time course assay.

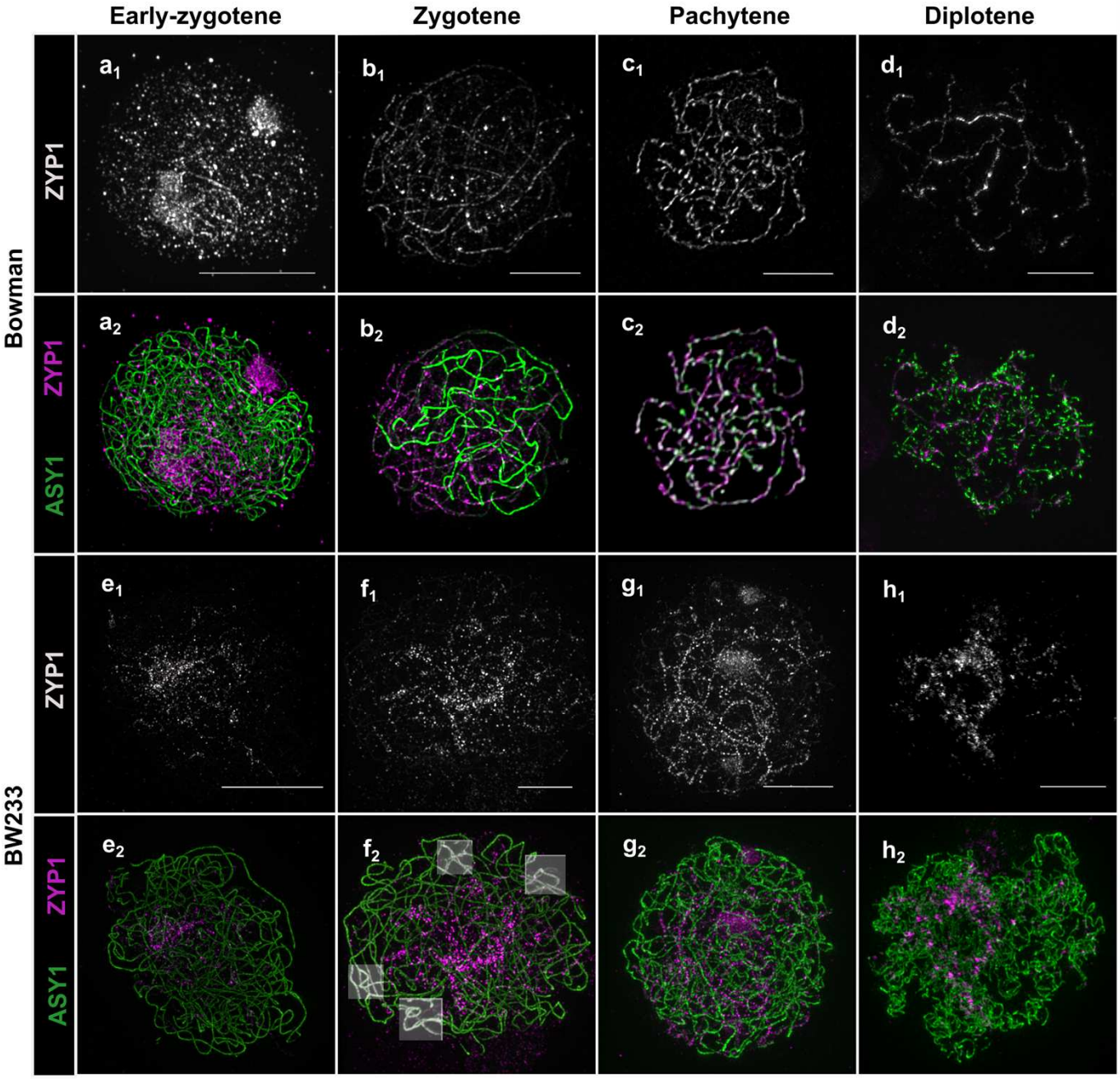

Figure 3: Synapsis in Bowman and BW233

(a-d) Normal synapsis progression in Bowman. a) ZYP1 polymerization starts at one side of the nucleus and elongates during b) zygotene stage. Homologous chromosomes are fully aligned via ZYP1 at c) pachytene and get separated at d) diplotene exhibiting normal tinsel chromosomes. e) Somewhat normal initiation of synapsis in BW233. f) zygotene cells of BW233 show abnormal elongation of the ZYP1 “cluster” and unresolved interlocks (highlighted boxes). g) BW233 pachytene-like cell showing persistent HvZYP1 “clustering”. h) BW233 diplotene cells exhibiting abnormal tinsel chromosomes. (a-h) ASY1: green, ZYP1: grey or magenta, scale bars 5 µm.

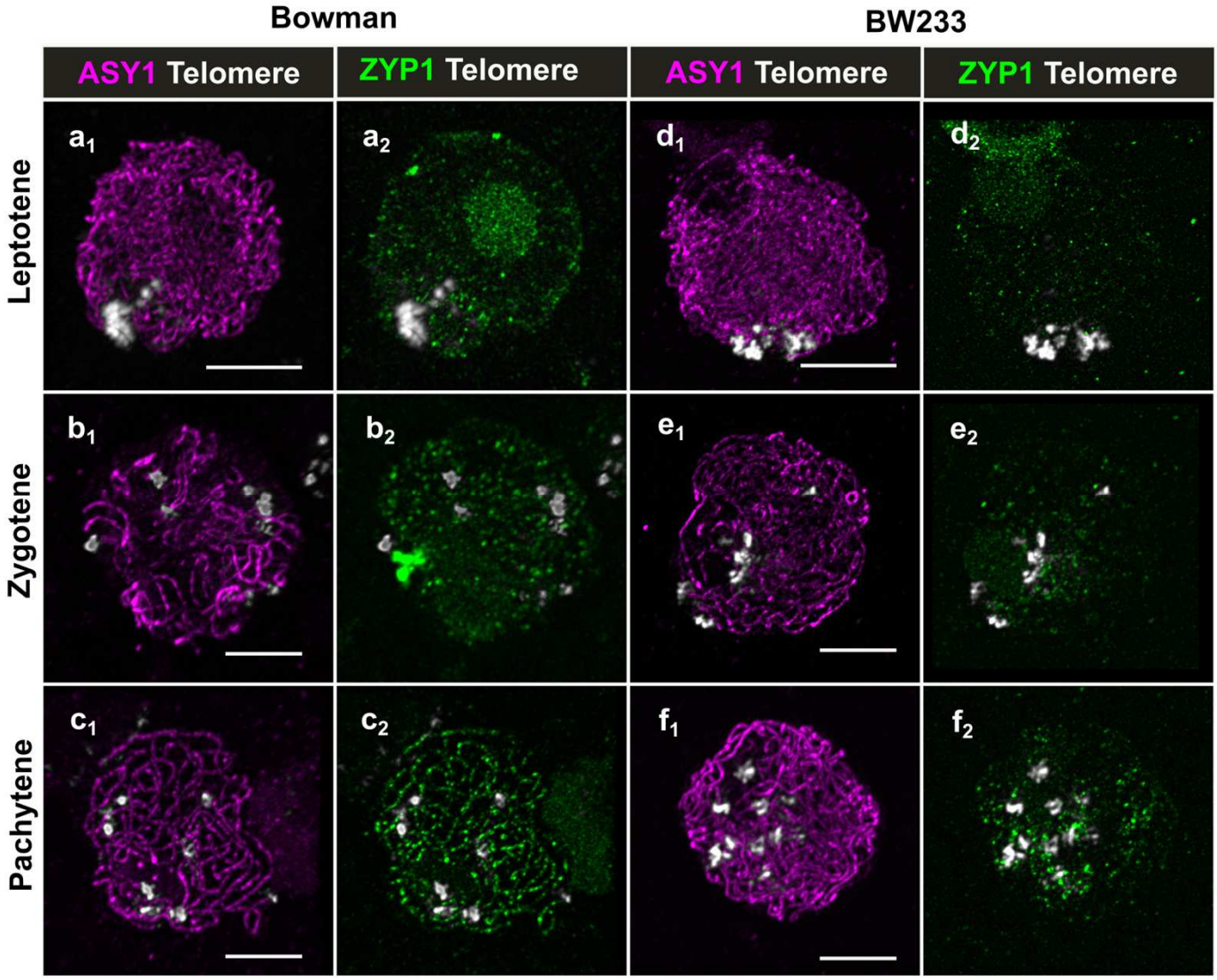

Figure 4. Telomere behaviour in Bowman and BW233
At leptotene stage, telomeres (grey) cluster at one side of the nucleus in both a) Bowman and d) BW233. As synapsis progresses from b) zygotene to c) pachytene stage, telomeres start to move around the nuclear periphery in Bowman. However, in BW233 e) zygotene and f) pachytene-like stage cells, they are still located at one side of the nucleus. Scale bar 5 µm

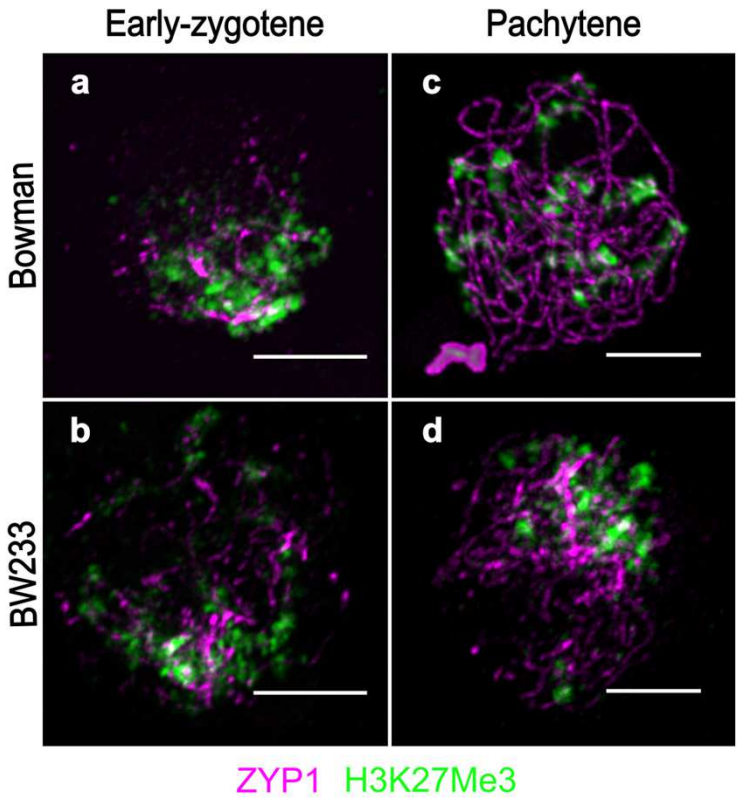

Figure 5. Chromatin behaviour and histone methylation in Bowman and BW233
At the beginning of ZYP1 (magenta) polymerization chromatin seems loose as shown by the diffuse H3K27me3 (green) around the telomere region in both a) Bowman and b) BW233. c) in Bowman at pachytene, the H3K27me3 signal is orderly allowing identification the telomeric regions. d) In BW233, the H3K27me3 signal is more diffuse as a result of abnormal synapsis. Scale bar 5um.

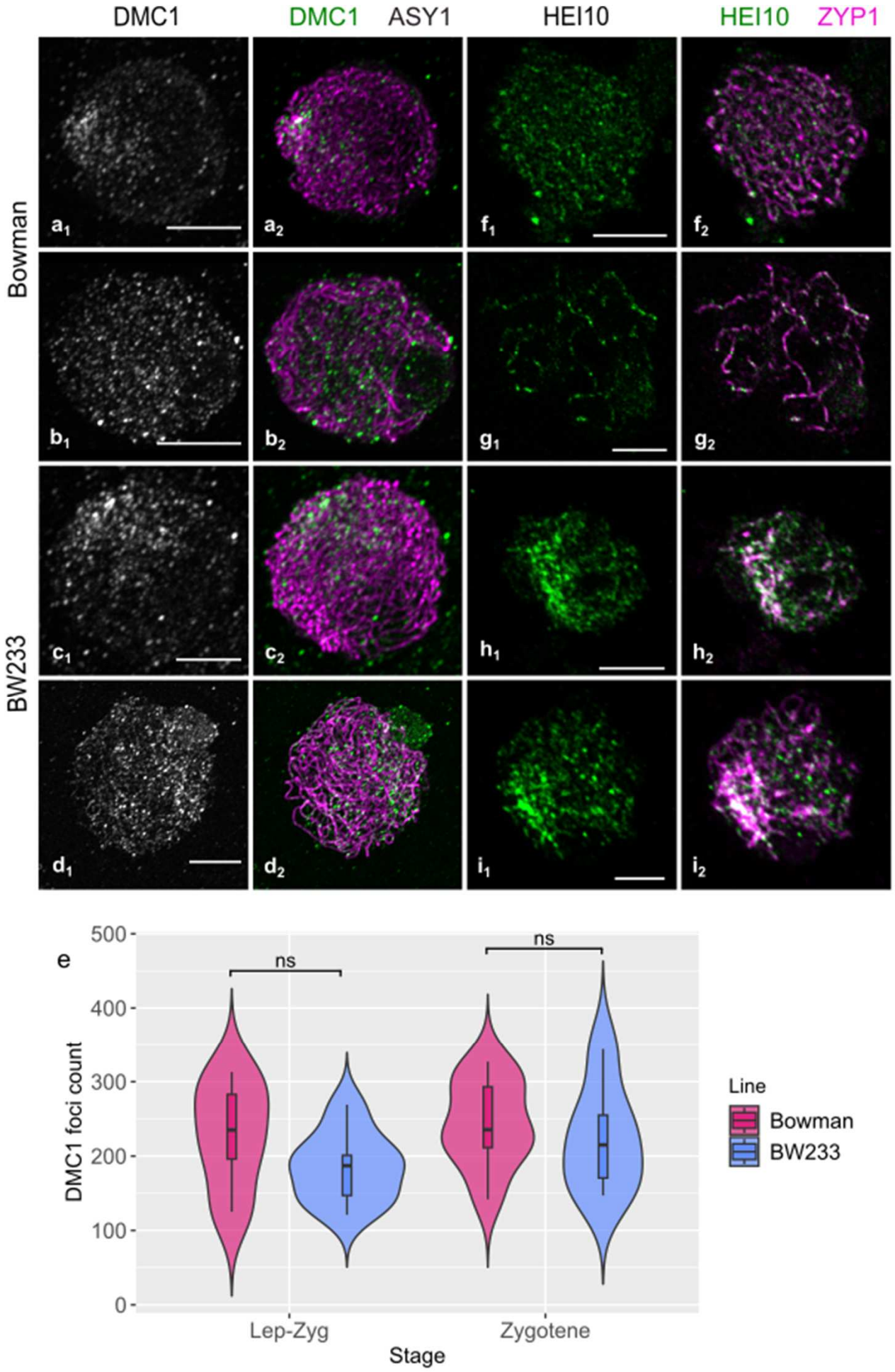

Figure 6: DMC1 and HEI10 behaviour in Bowman and BW233

At leptotene stage, DMC1 foci (green, grey) cluster at one side of the nucleus in a) Bowman and disperse along the ASY1 axes (Magenta) during b) zygotene. In BW233, we see the same behaviour at c) leptotene and d) zygotene. e) Violin plot of DMC1 foci count showing no significant difference between Bowman and BW233. HEI10 foci load on ZYP1 axes in both f,g) Bowman and h,i) BW233, but they resolve as large foci in g) bowman pachytene cells while they cluster around the ZYP1 polycomplex in h,i) BW233. scale bar 5µm

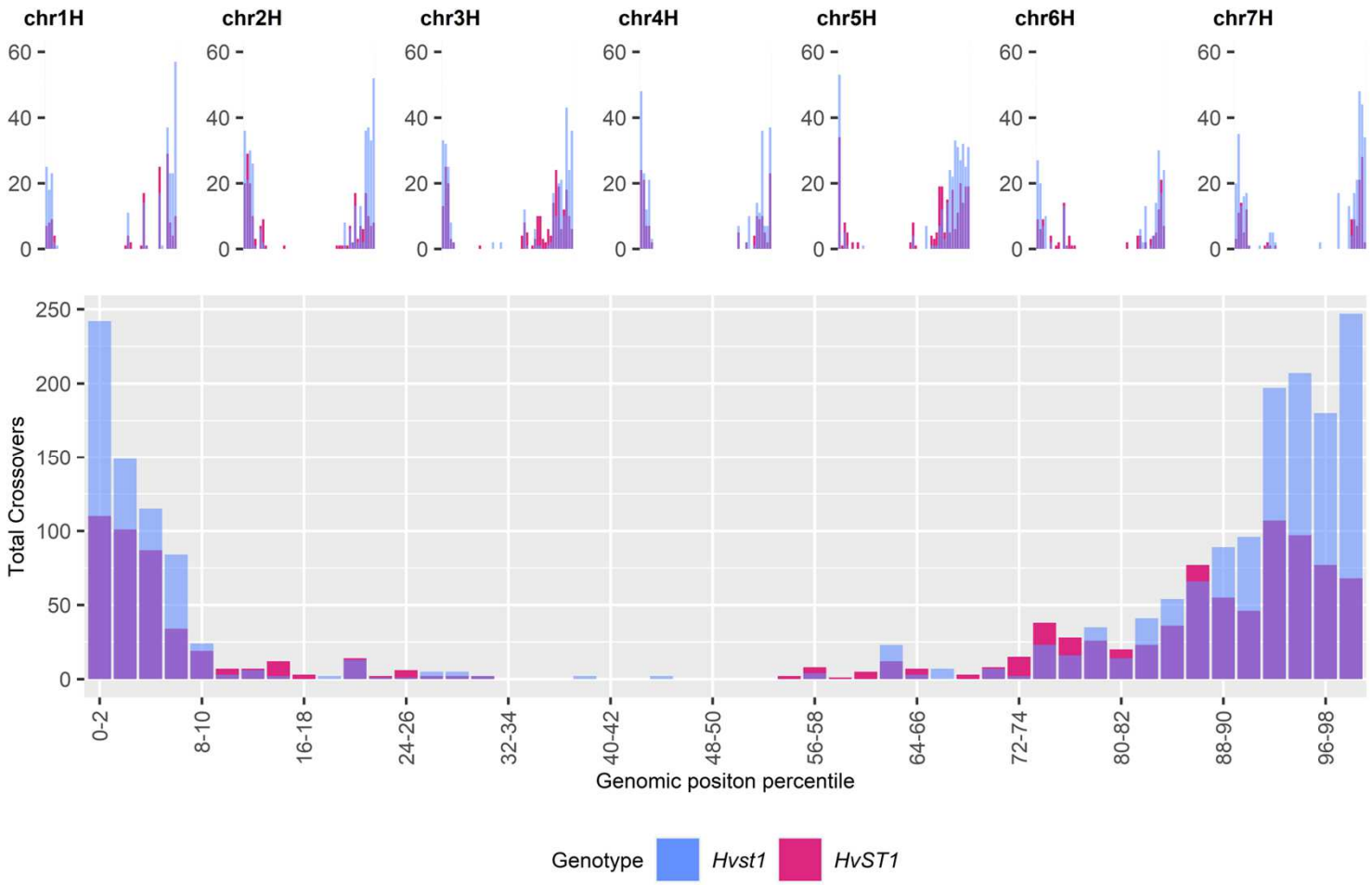

Figure 7: Recombination

Comparison of the total number of crossover events detected using 50K iSelect markers across all seven chromosomes (represented individually above and combined below) between *Hvst1* (in Blue; n=95) and *HvST1* (WT; in pink; n=95) per binned (2%) genomic position (Mbp) percentile.

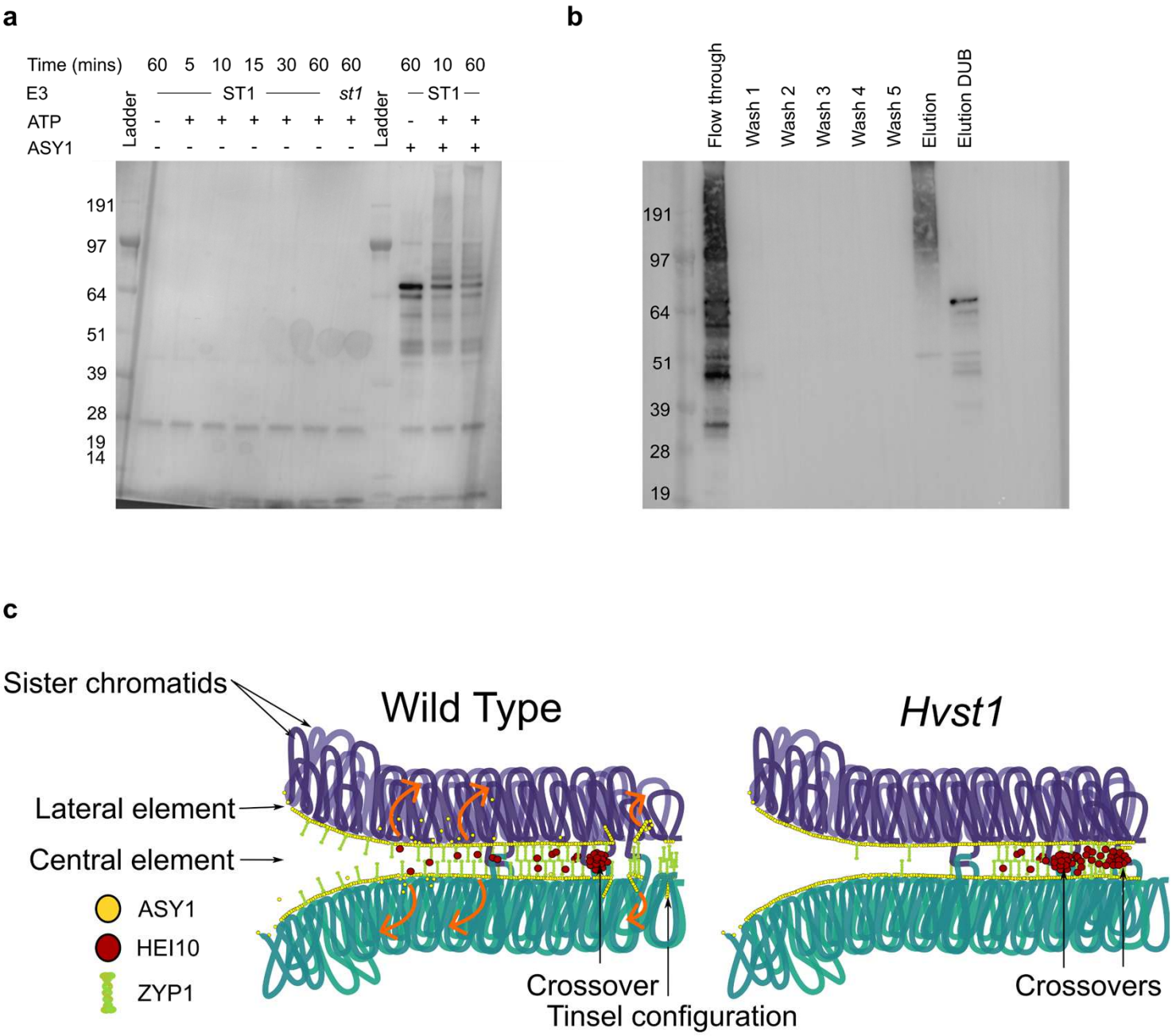

Figure 8. ASY1 ubiquitination and Model

a) Anti-ASY1 western blot of HvST1 autoubiquitination time course and HvST1-ASY1 substrate ubiquitination assay; lane description from left: 1-ladder; 2-HvST1 autoubiquitination no ATP control, 3-7: HvST1 autoubiquitination time course, 8: Hvst1 autoubiquitination control, 9: ladder, 10: HvST1-ASY1 substrate ubiquitination no ATP control, 11-12: HvST1-ASY1 substrate ubiquitination assay. b) Western blot of fractions recovered from GST-TUBE capture of polyubiquitinated products of HvST1-HvASY1 substrate ubiquitination assay probed with anti-HvASY1 antibody. HvASY1 antibody labels TUBE captured ubiquitinated protein in the eluted fraction and upon treatment of this fraction with broad spectrum deubiquitinating (DUB) enzyme ASY1 is returned to its original size (~64 KDa). Marker sizes in KDa are indicated on the left. c) proposed model of the role of HvST1 in synapsis (purple loops= homologue 1; sea green loops=homologue 2. In the wild type, synapsis is synchronized and ZYP1 polymerises between the two homologues dependent on continuous ASY1 turnover while the pro-crossover factor HEI10 diffuses along the ZYP1 axes. In Hvst1 mutants, ASY1 turnover is compromised leading to partial synapsis and formation of the ZYP1 cluster while diffusion of HEI10 is constrained to partially synapsed regions, affecting coarsening dynamics by increasing the subtelomeric concentration of HEI10, leading to more crossovers which are closer together in this region.